Fuel cell cathodes fabricated by the impregnation method

Performance and reaction mechanisms of solid oxide fuel cell cathodes fabricated by the impregnation method

By

QI ZHANG, B.E.

A Thesis
Submitted to the School of Graduate Studies
in Partial Fulfillment of the Requirements
for the Degree
Master of Applied Science

McMaster University

MASTER OF APPLIED SCIENCE (2008) McMaster University
MATERIALS SCIENCE AND ENGINEERING Hamilton, Ontario

TITLE: Performance and mechanism study of solid oxide fuel cell cathodes fabricated by the impregnation method
AUTHOR: Qi Zhang, B.E. (Tsinghua University)
SUPERVISOR: Dr. Anthony Petric
NUMBER OF PAGES: xvi, 101

Abstract

The exploration of cathode materials and fabrication methods plays an important role in the development of solid oxide fuel cell (SOFC) technology. The objective of this study is first to optimize the cathode microstructure by the impregnation method, and then investigate the potential application of copper manganese spinel as a new cathode material with optimized microstructure and explore the reaction mechanism of the cathodes.

The impregnation method was employed to fabricate a composite cathode with electrocatalyst particles dispersed in a framework of electrolyte material. The impregnation method is relatively easy to apply and yield the optimized microstructure, allowing extended three phase boundary length and absence of secondary phase formation during fabrication.

The polarization performance of copper manganese spinel (CMO) impregnated YSZ cathodes was examined by adjusting catalyst particle size, electrode thickness and catalyst content. A critical thickness of 16.9±2.0 μm for the CMO-YSZ composite cathode was calculated from Tanner's model. Decreased catalyst particle size and a thickness close to the critical value were found to eliminate polarization loss. The composite cathode with 50 wt% CMO impregnation showed a polarization resistance as low as 0.3 Ωcm^2 at 750°C. At 800°C, an SOFC with CMO-YSZ composite cathode had a power density of 172 mW/cm^2, which was 2.5 times higher than the cell with the traditional LSM-YSZ composite cathode under the same conditions.

The cathode reaction mechanism of CMO-YSZ and strontium doped lanthanum ferrite (LSCF) impregnated Gd doped ceria (CGO) composite cathodes was studied, using impedance spectroscopy, cyclic voltammetry and current interruption techniques. Surface diffusion and mass transfer were determined to be the rate controlling steps for CMO-YSZ composite cathode at low and high temperatures, respectively. A low frequency process at low temperatures and at least two processes at high temperatures were identified as rate determining steps of LSCF-CGO composite cathodes. A cathodic current activation effect was observed on CMO-YSZ cathode under current passage. The catalytic activity of CMO was enhanced by the cathodic current and the effect existed in both long-term and short-term experiments.

The results of this study suggest that copper manganese spinel has attractive properties as a new catalyst material for the cathodic reaction with the composite structure obtained by the impregnation method.

Acknowledgements

It is a pleasure to thank the many people who have helped and inspired me to make this thesis possible.

It is difficult to overstate my gratitude to my supervisor, Dr. Anthony Petric, for his guidance and support during my research and study. Thanks for his sound advice, encouragement, the trust and confidence he gave me throughout my research.

I wish to specially thank Dr. Boris Martin for his inspiration, generous help and good teaching to help initiate this work.

I was delighted to interact with Dr. Denise Gosselink and Dr. Jim Britten. Thanks for their helpful discussion with me. I am grateful to Rob Hughes, Jim Garret, Steve Koprich, Doug Culley, Wenhe Gong and Ed McCaffery and Chris Butcher for their invaluable technical assistance. I would like to thank Joshua Deng, Dr. Reza Bateni, Ping Wei, Amin Mali, Luz Quintero and Peter Rombos for all I learnt from them and the camaraderie they brought in the lab.

I thank my friends at McMaster University, especially in the MSE department, for providing an exciting, supportive, friendly and fun environment in which to learn and grow. I would like to thank Hao Xia for everything that we've been through.

I am grateful for the financial support of the Natural Sciences and Engineering Research Council of Canada and the collaboration with Tony Wood from Versa Power Systems Ltd.

Lastly, I wish to thank my parents and grandparents. Their endless love and support is always with me, no matter where I am. To them I dedicate this thesis.

Contents

List of Figures

List of Tables

Chapter 1

Introduction

1.1 Motivation and Objectives

Solid oxide fuel cell (SOFC) technology has achieved increasing technical refinement over more than fifty years of development. Large stationary power plants incorporating SOFC stacks have been demonstrated throughout the world. Yet the cost of today's state-of-the-art SOFC technology remains much too high to compete with entrenched power generation technologies. Forthcoming metal-supported SOFCs are expected to be competitive in the power generation equipment market because of the strength, tolerance to rapid thermal cycling and reduced materials cost that the metal-support provides. Introducing ferritic stainless steel to the materials set introduces a number of challenges that must be overcome before successful deployment of metal-supported SOFC technology. These challenges include Cr poisoning, achieving high performance at low operating temperature, and co-processing the metal-support and electrocatalysts (Tucker *et al.*, 2007). The traditional SOFCs composed of all ceramic components can be co-sintered at 1200-1400°C in air. However, co-sintering with metal support requires reduced temperature and reducing atmosphere to avoid oxidation of the metal. A similar issue is encountered when braze-sealing SOFCs. Metal supported SOFC technology enables the use of brazed seals and joints that can withstand extremely rapid thermal cycling (Tucker *et al.*, 2006). This offers the promise of rapid SOFC startup, and tolerance to large thermal gradients. Brazing requires a vacuum or inert atmosphere, however, and is therefore incompatible with cathode catalysts as well. There have been many studies towards overcoming the above problems by new kinds of fabrication methods. An infiltration (impregnation) process has been developed by Virkar *et al.* (1996) that allows the cathode catalyst to be introduced to the cathode structure after the co-sintering and brazing steps.

In addition to the fabrication techniques, developing a catalyst material having high catalytic activity at reduced temperatures is of comparable importance in lowering the cost of SOFC operation. The efficiency of the traditional strontium-doped lanthanum manganite falls off significantly with decreasing temperature, and hence great efforts have been made to explore cathode materials to meet the requirements at intermediate temperatures.

This thesis will review the various advances made in improving the cathode performance through the development of copper manganese spinel as a cathode material and the impregnation method. The impregnation method has been widely used for the fabrication of SOFC electrodes, but few have focused on the copper-manganese spinel as the catalyst material or Gd doped ceria (CGO) as the electrode framework. Copper-manganese spinel has shown properties suitable for a cathode material and CGO has been used widely as the electrolyte for intermediate temperature SOFCs with other fabrication methods. This thesis concentrates on the development of the copper-manganese spinel-YSZ composite cathode and LSCF-CGO composite cathode fabricated by the impregnation method. The objectives of the thesis are listed as follows:

1. To fabricate the composite cathode with the optimized microstructure by the impregnation method.
2. To measure the catalytic properties of the fabricated cathodes and resolve the optimization strategy.
3. To identify the cathodic reaction mechanism of the copper-manganese spinel in the composite structure.

1.2 Organization of the thesis

The solid oxide fuel cell and cathode background is surveyed briefly in the second chapter, with particular attention paid to the impregnation method to fabricate the state-of-the-art cathode. Chapter three introduces the cell fabrication processes, especially the composite cathode fabrication. Chapter four details the experimental approaches employed in the study to characterize the structure and electrochemical performance of the cathodes. The structural characterization of the CMO-YSZ and LSCF-CGO composite cathodes are reported in chapter five. Chapter six presents the polarization behavior of the CMO-YSZ cathodes with the effect from electrode thickness, catalyst particle size and content in the composite layer as well as the power density. In chapter seven, the cathode reaction mechanism at the CMO-YSZ and LSCF-CGO composite cathodes are discussed and the current activation of CMO-YSZ is explored as well.

Chapter 2

The Solid Oxide Fuel Cell Cathode

2.1 SOFC overview

Fuel cells are the most efficient devices yet invented for the conversion of chemical energy into electrical energy by electrochemical combination of a fuel with an oxidant. A fuel cell consists of two electrodes (the anode and cathode) separated by an electrolyte. Fuel (e.g., hydrogen) is fed to the anode where it is oxidized and electrons are released to the external (outer) circuit. Oxidant (e.g., oxygen) is fed to the cathode where it is reduced and electrons are accepted from the external circuit. The electron flow (from the anode to the cathode) through the external circuit produces direct-current electricity. The basic reactions involved in a fuel cell operation are shown as follows:

$$\text{Anode} : \mathrm{H_2} \rightarrow 2\mathrm{H} + 2\mathrm{e}^- \tag{2.1}$$

$$\text{Cathode} : \frac{1}{2}\mathrm{O_2} + 2\mathrm{e}^- \rightarrow 2\mathrm{O}^{2-} \tag{2.2}$$

$$\text{Overall}: H_2 + \frac{1}{2}O_2 \rightarrow H_2O \tag{2.3}$$

The electrolyte conducts ions between the two electrodes. Practical fuel cells are not operated as single units; rather, they are connected in electrical series to build output voltage. A series of cells is referred to as a stack.

According to the type of electrolyte, fuel cells can be sorted as Proton Exchange Membrane Fuel Cells (PEMFC), Phosphoric Acid Fuel Cells (PAFC), Alkaline Fuel Cell (AFC), Molten Carbonate Fuel Cell (MCFC) and Solid Oxide Fuel Cell (SOFC).

Solid Oxide Fuel Cells have several distinct advantages over other types of fuel cells, e.g., use of non-precious materials, no liquids involved in the cell, and no compositional change in the electrolyte. The use of a solid electrolyte in ceramic fuel cells eliminates material corrosion and electrolyte management problems. Ceramic fuel cells are generally operated at temperatures above 600°C.

In present fuel cells, the electrolyte of choice is zirconia, stabilized by 8 mol% Y_2O_3 (8YSZ). YSZ has many advantages to make it the most suitable material at present: good ionic conductivity, low electronic conductivity, chemical stability and non-toxicity. Another electrolyte material of interest is Gd doped CeO_2 (GCO). GCO is regarded as a better electrolyte for intermediate temperature solid oxide fuel cells according to some investigations (Steele, 2000). However, GCO suffers loss of efficiency from electronic leakage.

The electrodes must possess high electrical conductivity, high catalytic activity, large surface area and compatibility with the electrolyte and interconnect. Nickel-YSZ cermet is the most commonly used anode material. Ni-YSZ anode allows a rapid and clean connection with the fuel and is of high electronic conductance. The drawback is that carbon deposition on Ni occurs at high carbon activities in the fuel and the reaction is blocked. On the other hand, Ni plays an active role in the reforming of carbon containing fuels. The cathode material is very important because the oxidation reaction mostly determines the efficiency of the fuel cell. $La_{0.8}Sr_{0.2}MnO_3$ has been the most widely used cathode material for high temperature SOFCs. Other materials, such as doped lanthanum cobaltite and doped lanthanum ferrite, are used with ceria based electrolytes for intermediate temperature SOFCs.

2.2 Requirements of the Cathode

The electrochemical reduction of the oxidant takes place at the cathode, and thus there are several critical requirements for the cathode material.

(1) Stability. The cathode must have a stable microstructure over the long term operation of a fuel cell. There must be an absence of disruptive phase transformations of the cathode material between room temperature and the fabrication temperature, to make it chemically and thermally stable.

(2) Conductivity. In order to support sufficient electron flow in the cell operating environment, the cathode material must have moderate electronic conductivity in the oxidizing environment at high temperature.

(3) Compatibility. The cathode must be thermally and chemically compatible with other components of the cell. The thermal expansion coefficient of the cathode material must be close to that of the electrolyte and interconnect material, to avoid cracking and disintegration. Meanwhile, chemical reaction between the cathode material and the adjoining components should also not occur, because

the second phase produced from any reaction may lead to degradation of the cathode performance.

(4) Catalytic activity. The main function of the cathode is to accelerate the reduction of oxygen, so it must possess sufficient catalytic activity for the oxygen reduction reaction.

In addition to the above requirements, it is also important for the cathode to have suitable porosity, ease of fabrication and low cost.

2.3 Cathode Material

2.3.1 Traditional Cathode Materials

Under the constraints of the cathode, strontium-doped lanthanum manganite (LSM) has been the most commonly used cathode material for SOFCs. LSM has sufficient electronic conductivity and a good thermal expansion coefficient (TEC) match with the YSZ electrolyte. For instance, the electronic conductivity of $La_{0.8}Sr_{0.2}MnO_3$ is around 175 S/cm between 700°C and 800°C and the TEC is 12.4 ppm/K (Minh, 1995). $La_2Zr_2O_7$ phase forms at the interface between LSM and YSZ at high temperatures ($> 1200°C$), which leads to the degradation of cathode performance. The formation of $La_2Zr_2O_7$ phase has been successfully avoided by optimizing the cathode fabrication techniques, which decreases the sintering temperatures of LSM and lowers the activity of La. Typically $(La, Sr)_{0.98}MnO_3$ is used.

$La_{1-x}Sr_xCoO_3$ (LSC) and $La_{1-x}Sr_xFeO_3$ (LSF) have been widely studied in recent years to be used as the cathode material for intermediate temperature SOFCs (ITSOFCs). Although they possess considerable oxide ion conductivity and sufficient electronic conductivity between 600°C and 800°C (Tai *et al.*, 1995; Skinner, 2001), they have a strong tendency to react with yttria-stabilized zirconia (YSZ) to form insulating zirconate phases at the cathode electrolyte interface during sintering. Meanwhile, the thermal expansion coefficient (TEC) of doped LSC is reported to be between 15-25 ppm/K, which is much higher than the TEC of YSZ (10.4 ppm/K) (Minh, 1995).

2.3.2 Copper Manganese Spinels

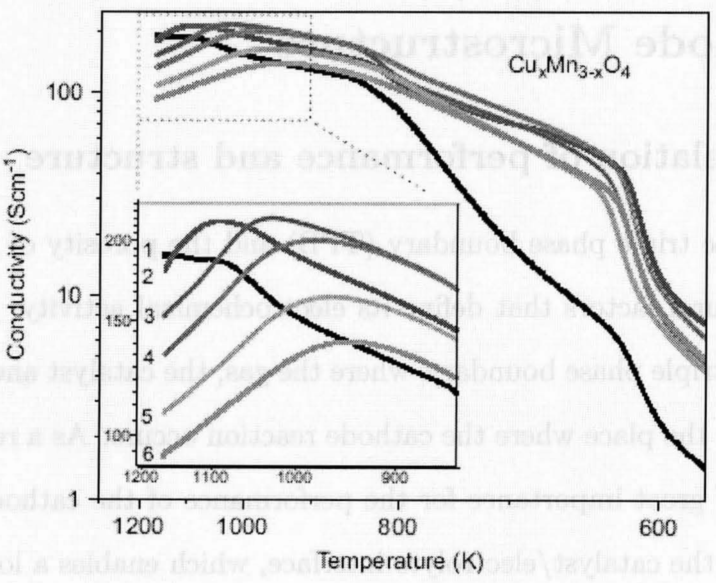

Figure 2.1: Arrhenius plot of conductivity for $Cu_xMn_{3-x}O_4$. Each curve is labeled in the insert: (1) x=1.08, (2) x=1.19, (3) x=1.28, (4) x=1.38, (5) x=1.47,(6) x=1.58.

The essential electrical and thermal properties of $Cu_xMn_{3-x}O_4$ with x varying between 1.00 and 1.60 was studied by Martin (2007). The thermal expansion behavior of the copper manganese non-stoichiometric compounds was characterized. Although the characterization was not performed for each composition, the few samples tested showed that the non-stoichiometric compounds presented a larger coefficient of thermal expansion, matching that of YSZ (Martin, 2007). The TEC of $Cu_{1.3}Mn_{1.7}O_4$ was reported to be 12.2 ppm/K at 25-1000°C (Petric & Ling, 2007). The electrical conductivity was measured for six compositions ranging from x=1.08 to 1.58 (Fig. 2.1). From Fig. 2.1, the value of x for the highest electrical conductivity is between 1.19 and 1.28 between 900 and 1000 K, which is the general operating temperature range for ITSOFCs. Due to the above considerations, $Cu_{1.25}Mn_{1.75}O_4$ was chosen to be investigated as the cathode material in this study.

2.4 Cathode Microstructure

2.4.1 Correlation of performance and structure

The length of the triple phase boundary (TPB) and the porosity of the cathode are two main structural factors that define its electrochemical activity. As discussed in Section 2.5, the triple phase boundary, where the gas, the catalyst and the electrolyte are in contact, is the place where the cathode reaction occurs. As a result, the length of the TPB is of great importance for the performance of the cathode. Large intergrain contact at the catalyst/electrolyte interface, which enables a long TPB length, favours the electrochemical oxygen reduction reaction. Another structural factor having strong influence on the cathode performance is the porosity. Porosity is important for the supply of oxygen to the TPBs, which can occur via O_2 molecules through pores in the cathode layer, or via adsorbed O atoms in a diffusion process (Østergård *et al.*, 1995). High porosity and large pore size will allow sufficient gas supply, but have detrimental effects on the conductivity of the cathode.

Using composite cathodes made from a mixture of electronic and ionic conductive materials, e.g. LSM and YSZ, has proven to be effective to obtain enlarged TPBs and sufficient porosity. Porosity can be well controlled by the sintering time, addition of carbon or other organic materials in the mixture, etc. Co-sintering of the catalyst and electrolyte materials tends to produce resistive secondary phases, due to the high sintering temperature of the electrolyte material. For instance, resistive $La_2Zr_2O_7$ and $SrZrO_3$ phases may form at the catalyst/electrolyte interface during fabrication if sintering at 1100-1400°C (Van Roosmalen & Cordfunke, 1992; Chen *et al.*, 1993). The limitations of the high temperature sintering step leaves challenges for the development of the composite cathode by the conventional ceramic mixing method.

2.4.2 The impregnation method

In recent years, the impregnation method has been developed to overcome the problems caused by the conventional ceramic coating methods for SOFC electrodes. The wet impregnation method (infiltration method) is one of the approaches employed to synthesize the cathode by the deposition of nano-particles into an established electrode framework. The procedure of the impregnation method is shown in Fig. 2.2.

Recent studies on the impregnation method can be divided into three choices of material for the framework (Sholklapper *et al.*, 2007a): a) catalyst material, b) electrolyte material and c) catalyst-electrolyte composite. In the first category, GDC-impregnated $La_{0.8}Sr_{0.2}MnO_3$ (LSM) electrode (Fig. 2.3) was reported to have a polarization resistance of 0.21 Ωcm^2 at 700°C by Jiang & Wang (2005). An LSM-$Sm_{0.2}Ce_{0.8}O_{1.9}$ (SDC) composite cathode was fabricated by impregnating an LSM framework with $Sm_{0.2}Ce_{0.8}O_{1.9}$ by Xu *et al.* (2006). The interfacial polarization resistance of 50 wt% SDC impregnated LSM cathode was 0.23 Ωcm^2 at 700°C.

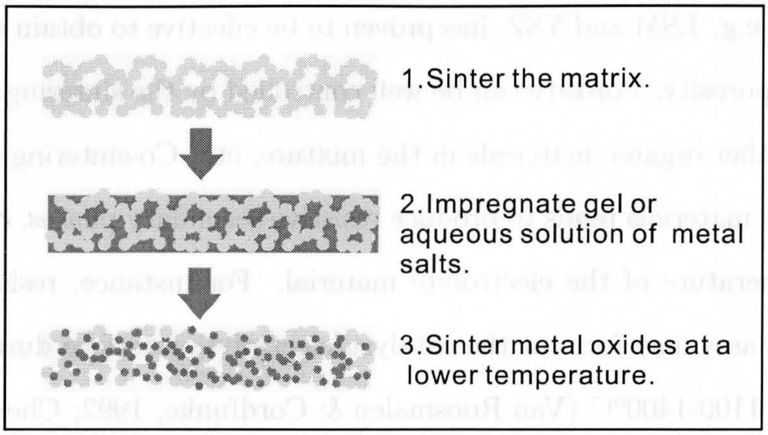

Figure 2.2: The procedure for the impregnation method.

Mixed conducting $La_{1-x}Sr_xCo_{1-y}Fe_yO_3$ was selected as the backbone material and impregnated with $Y_{0.2}Ce_{0.8}O_{1.9}$ (YDC) nanoparticles to form a composite cathode by Sholklapper *et al.* (2007a). The ohmic and interfacial resistances were both decreased compared to the same cathode without impregnation. In the second category, several efforts have been made to impregnate a ZrO_2-based electrolyte framework with LSM (Huang *et al.*, 2005; Sholklapper *et al.*, 2007b; Huang *et al.*, 2006; Tucker *et al.*, 2007). Huang *et al.* (2006) impregnated YSZ matrices with LSM from molten salt, aqueous solution and nano particles. LSM-YSZ composite cathodes exhibited polarization resistance between 0.4 and 0.5 Ωcm^2 at 700°C. Composite electrodes were prepared by adding 40 wt% $La_{0.8}Sr_{0.2}MnO_3$ into porous YSZ by Wang *et al.* (2007). The LSF-YSZ cathode calcined at 850°C showed an initial area specific resistance (ASR) of 0.13 Ωcm^2 at 700°C, but the ASR increased linearly with time to 0.55 Ωcm^2 after 2500 h. Sholklapper *et al.* (2006) prepared a 6 wt% LSM impregnated YSZ cathode (Fig. 2.4) by a single-step infiltration method. The maximum power density of the cell was 0.27 W/cm² and the polarization resistance of the cathode was ~2.9 Ωcm^2 at 700°C. In the third category, Co_3O_4, $Sm_{0.6}Sr_{0.4}CoO_{3-\delta}$ (SSC) and LSF

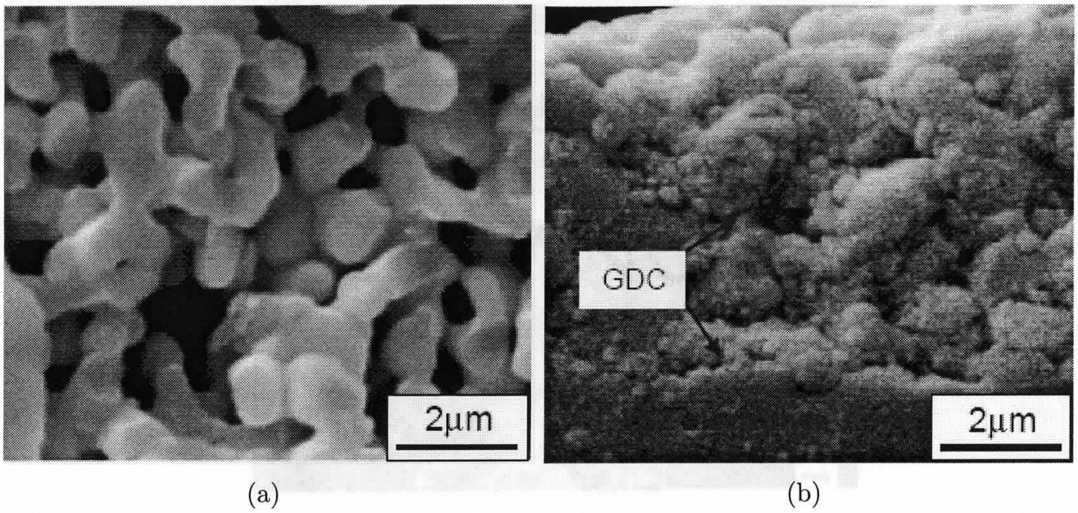

(a) (b)

Figure 2.3: SEM images of fractured cross-sections of (a) LSM framework, and (b) GDC impregnated LSM electrode after fuel cell testing. (Jiang & Wang, 2005)

nanoparticles were infiltrated into LSM-YSZ preformed cathodes (Sholklapper *et al.*, 2007a; Yamahara *et al.*, 2005; Lu *et al.*, 2006). The catalytically active nanoparticles substantially improved the preformed cathode performance. With the impregnated SSC nanoparticles in the LSM-YSZ cathode, the polarization resistance was decreased from ~19.8 to 8.5 Ωcm^2 and the maximum power density increased from 80 to 153 mW/cm^2 at 600°C (Fig. 2.5) (Lu *et al.*, 2006).

The cathode with catalyst material as the matrix allows high electronic conductivity. However, this kind of cathode has very few choices for the framework material due to the limits of its TEC and chemical compatibility with the electrolyte. The composite cathode with electrolyte material can overcome the TEC mismatch problem but still leaves the challenge of choosing the catalyst material to achieve acceptable electrochemical performance. The cathode with catalyst-electrolyte composite as the framework is a compromise between the two methods, but the addition of the third phase nanoparticles requires careful control of the fabrication procedures

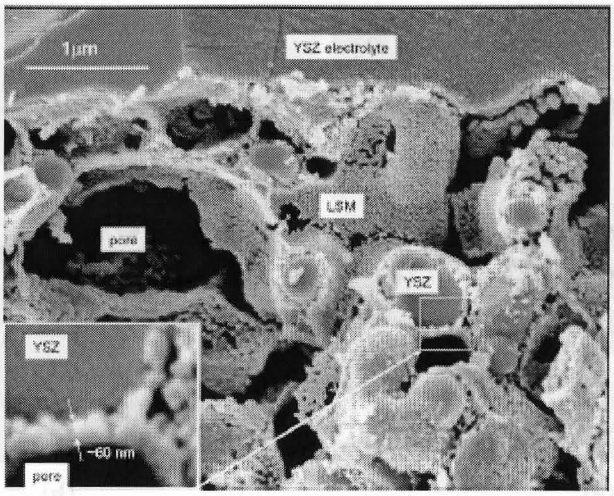

Figure 2.4: Cross-sectional SEM images of an infiltrated LSM-YSZ cathode. (Sholklapper *et al.*, 2006)

to avoid reaction among the phases.

2.5 Cathode Reactions

The overall reaction for the oxygen reduction at the cathode can be written as (Minh, 1995):

$$\mathrm{O_2} + \mathrm{V_O''} + 2\mathrm{e^-} = \mathrm{O_O^x} \tag{2.4}$$

The reaction involves several processes, including gas diffusion, adsorption and dissociation of oxygen, diffusion of adsorbed oxygen, diffusion of dissolved oxygen in the electrolyte and charge transfer across the electrode/electrolyte phase boundary (Minh, 1995). Each of them can be the possible rate determining step, depending on the cathode structure, material and experimental conditions.

The possible reaction paths of the oxygen reduction and incorporation reaction were given by Fleig (2003), shown in Fig. 2.6. The electrode surface path

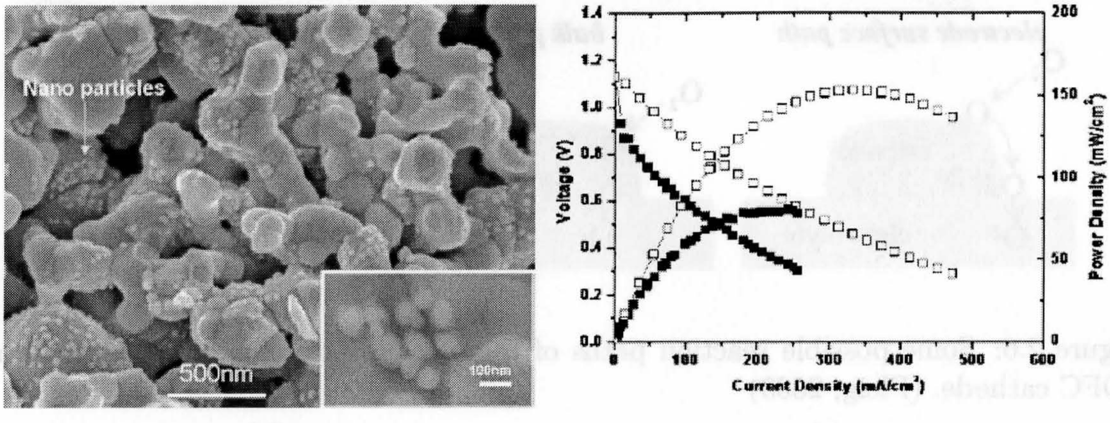

(a)

(b)

Figure 2.5: (a) SEM image of a porous LSM-YSZ cathode with infiltrated nano SSC particles, (b) Performance curves for the cell without (■) and with (□) nano SSC particles in an LSM-YSZ cathode at 600°C. (Lu *et al.*, 2006)

includes oxygen gas diffusion, adsorption of oxygen on the electrode surface, diffusion of oxygen species along the surface toward the three-phase boundary (TPB), where electrolyte, electrode, and gas phase meet, followed by complete ionization and ionic transfer into the electrolyte. The incorporation into the electrolyte does not necessarily occur directly at the TPB. Surface or interface diffusion of the ionized species could lead to a certain broadening of the incorporation zone. The bulk path consists of oxygen gas diffusion, adsorption on the cathode surface, dissociation and ionization, incorporation into the cathode, oxide ion transport through the electrode, and the transfer of the ion into the electrolyte. The electrolyte surface path includes oxygen gas diffusion, adsorption, and ionization on the electrolyte surface, followed by a direct incorporation into the electrolyte. The very low electronic conductivity of typical electrolytes (particularly of zirconia) can be expected to restrict the active zone to a region very close to the TPB. Hence, this path is, from a geometrical point of view, similar to the electrode surface path discussed above.

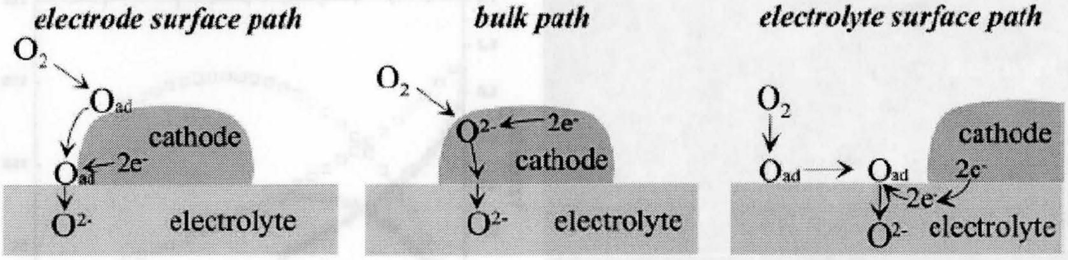

Figure 2.6: Some possible reaction paths of the oxygen reduction and transport at SOFC cathode. (Fleig, 2003)

The cathodic reaction (2.4) can simultaneously occur via all three paths, and for each path one or more elementary steps determine the corresponding reaction rate. The path with the fastest rate-determining step dominates the overall reaction rate. The paths also can affect each other.

2.6 Polarization mechanisms at SOFC cathodes

Polarization is the voltage loss at the electrode. Different types of polarizations are shown in the schematic plot of voltage versus current density in Fig. 2.7 (Minh, 1995). Electrode polarization causes large voltage loss in SOFCs and needs to be minimized to increase the efficiency. Activation polarization is due to the sluggishness of reactions occurring at the electrode-electrolyte interface. The ohmic polarization stems from resistance to electron and ion flow in materials and is generally dominated by the electrolyte resistance. Concentration polarization is caused by the resistance to gas transport through the electrode pores and interfaces. Details of the three polarizations are discussed in the sections below.

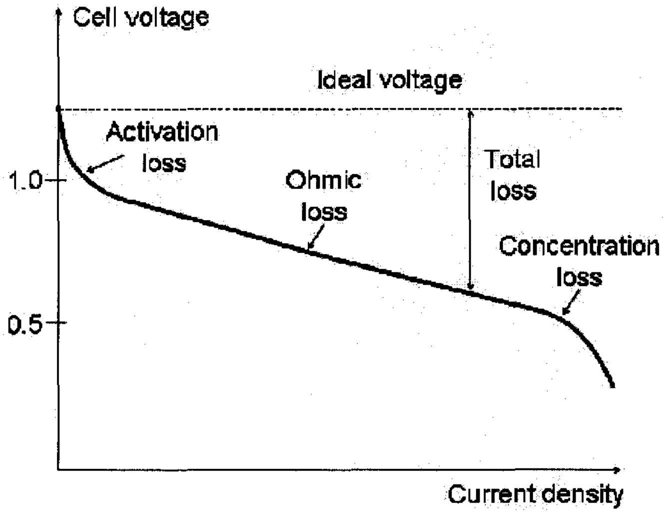

Figure 2.7: Schematic plot of voltage versus current density showing different types of polarizations.

2.6.1 Activation polarization

Activation polarization is the energy barrier for the electrochemical reaction to occur. The activation potential can be considered to be the extra potential required to reduce the activation energy barrier of the rate limiting step to a value such that the cathode reaction proceeds at the desired rate. Which part of the overall oxygen reduction reaction constitutes the rate-limiting step depends upon cell design and operating point: it could be related to adsorption of oxygen onto the surface of the cathodes, electron transfer, desorption of oxygen ions or many other factors.

Activation polarization can be expressed by the Butler-Volmer Equation:

$$i = i_o \left[\exp\left(\frac{n\alpha F\eta}{RT}\right) - \exp\left(\frac{-n(1-\alpha)F\eta}{RT}\right) \right] \tag{2.5}$$

where i is the absolute current flow through the interface, i_o is the equilibrium exchange current density, η is the overpotential, n is the number of charge carriers transferred in the reaction, α is the charge transfer coefficient and F/RT has its usual meaning. High exchange current densities mean high electrochemical reaction rate and hence the possibility of good cathode performance.

When the activation polarization is high, the second term on the right hand side of Equation 2.5 is much smaller than the first and hence can be neglected. By taking the natural logarithms of both sides and rearranging, the Tafel Equation is obtained:

$$\ln(i) = \ln(i_0) + \frac{n\alpha F\eta}{RT} \tag{2.6}$$

The exchange current density i_0 can be determined experimentally by extrapolating plots of $ln(i)$ versus η to $\eta = 0$. The exchange current density represents the electrode reaction rate, and hence is an important parameter in evaluating the polarization of an electrode.

2.6.2 Ohmic polarization

The ohmic polarization (resistance polarization) is the loss associated with the transport of charge carriers (electrons and ions) through the electrodes and electrolyte. The conduction of ions through the electrolyte, the transport of electrons through the electrodes and current collectors and contact resistance between cell components all contribute to the ohmic polarization.

2.6.3 Concentration polarization

Concentration polarization is the loss associated with concentration variation of critical species from mass transport. Diffusion of reactants and products in the electrodes is the main contribution for the concentration polarization. At the cathode, concentration polarization is related to the transport of O_2 and N_2. The gaseous transport is a function of the fundamental binary diffusivity, $D_{O_2-N_2}$, and cathode microstructure. The magnitude of the oxygen flux must be matched to the rate of electrochemical reaction, and in turn, to the current density drawn from the cell. At low current density, concentration polarization losses are typically small in SOFCs. It becomes more severe as the degree of conversion increases.

Chapter 3

Sample Fabrication

3.1 Electrolyte preparation

Polycrystalline YSZ electrolytes were fabricated by uniaxially pressing a submicron-size, 8 mol% yttria stabilized zirconia powder (TZ-8Y, TOSOH ceramics, Japan). The YSZ powder was mixed with 7 wt% of 5% polyvinyl alcohol (PVA) aqueous solution binder in a mortar and dried in the oven for 24 h before pressing. The powder was compacted in a 32 mm diameter steel die (6 grams of powder per pellet), using 900 MPa pressure. The samples were sintered in air at 1500°C for 20 h to obtain fully dense, 25 mm diameter, 1.90 mm thick pellets. The sintered wafers were mounted on cylindrical steel holders with thermoplastic glue (CrystalBond 590, Washbury Adhesives, U.S.A.) for polishing on a Struers Roto-System 300 automatic polisher. The microstructure of the fabricated YSZ electrolyte is shown in Fig. 3.1(a).

Polycrystalline Gd doped ceria (CGO) electrolytes were fabricated by uniaxially pressing a nano-size, 20 mol% Gd doped ceria powder (Nextech Materials, USA). The CGO powder was calcined at 700°C in air for 7 h before pressing. The powder

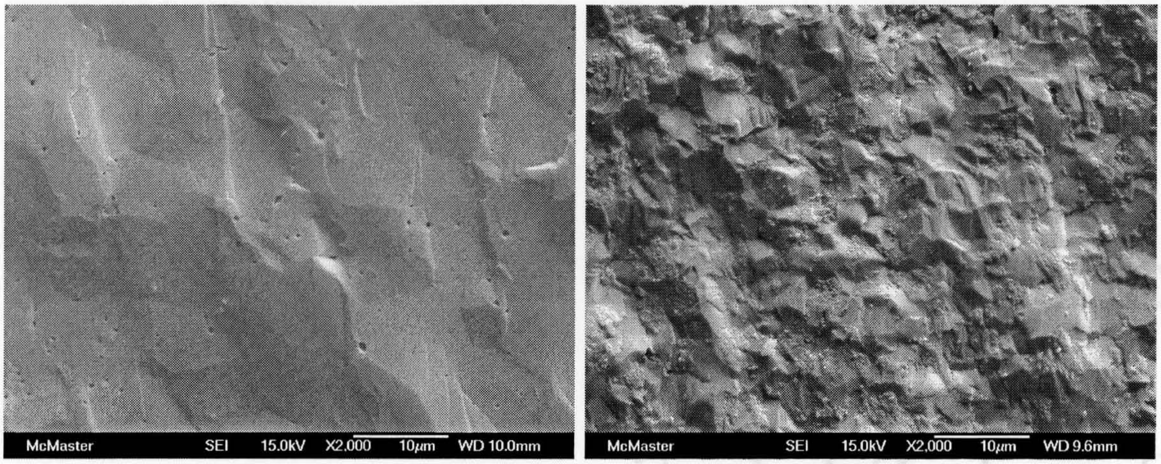

(a) (b)

Figure 3.1: SEM image of the fracture surface of (a) YSZ pellet and (b) CGO pellet.

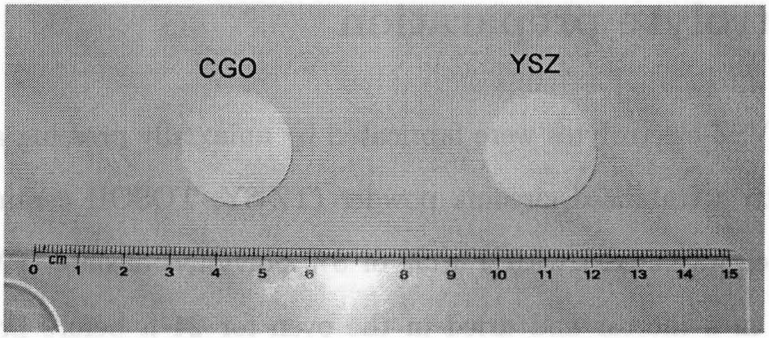

Figure 3.2: Appearance of the YSZ and CGO electrolyte pellets.

was compacted in a 32 mm diameter steel die (5.5 grams of powder per pellet), using 800 MPa pressure. The pellets were sintered in air at 1500°C for 20 h to obtain a dense pellet. The sintered CGO pellets were ~2.39 cm in diameter and ~1.99 mm thick. The sintered wafers were hand-polished to obtain a smooth surface, using #400 and #1200 polishing paper. Fig. 3.1(b) shows a cross-sectional view of the microstructure of the CGO electrolyte. The appearance of the YSZ and CGO electrolytes is shown in Fig. 3.2.

3.2 Cathode Framework Deposition

The cathode framework was deposited on top of the electrolyte pellet by screen printing. YSZ and CGO powder were mixed with screen printing oil and 20 wt% carbon powder, respectively. The carbon powder's average particle size and content in the slurry were chosen to obtain the desired porosity of the framework. The oil to powder ratio was adjusted to obtain a properly flowing ink. The amount of oil required was a function of the powder particle size, and was adjusted for each slurry. After screen printing, the YSZ film was sintered at 1300°C in air for 2 h and the CGO film was sintered at 1400°C in air for 2 h to form the cathode framework with the desired porosity. The microstructure of the YSZ and CGO framework is shown in Fig. 3.3. The porous framework was 10 mm in diameter and ~10-20 μm thick. The porosity of the structure is ~50-60%.

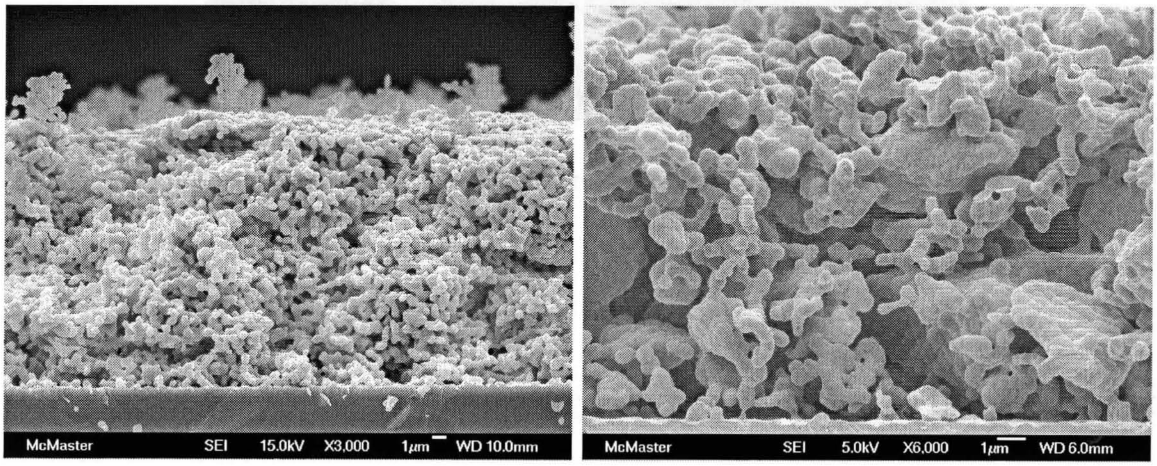

(a) (b)

Figure 3.3: SEM images of the cross section of the electrolyte framework: (a) YSZ and (b) CGO.

Anode supported fuel cells for power density measurements were fabricated by depositing the YSZ framework on half cells provided by Versa Power Systems Ltd. The half cell was composed of a porous Ni-YSZ cermet anode and a dense YSZ electrolyte film. The cell pellet was 1.9 cm in diameter and 1 mm thick. SEM observation (Fig. 3.4) reveals that the YSZ framework was well sintered to the half cell by the same fabrication method used for the homemade electrolyte discs.

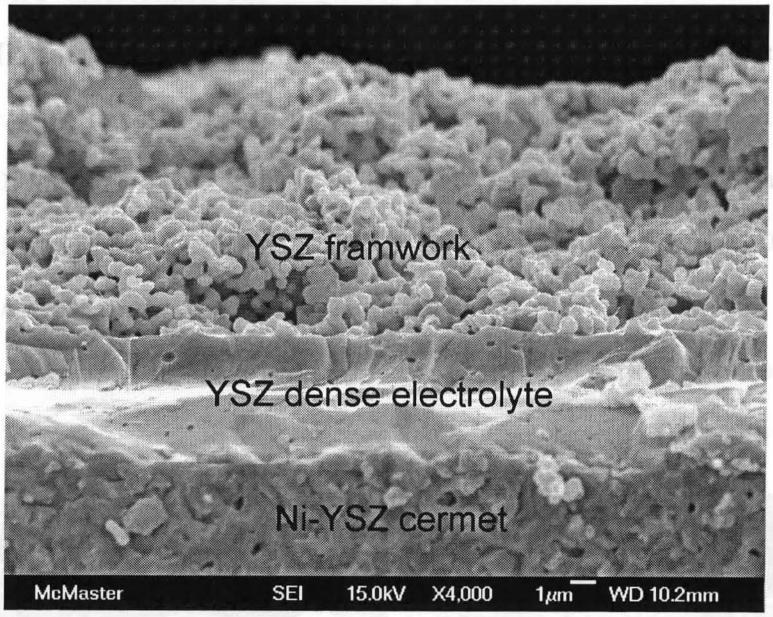

Figure 3.4: SEM image of the cross-section of a YSZ framework sintered on top of the half cell's electrolyte layer.

3.3 Catalyst Impregnation

The catalyst particles were deposited into the preformed cathode framework by impregnating the metal salt containing gel. Three steps are involved in the process: preparing a gel with proper viscosity, infiltration of the gel into the framework and sintering. Each step will have an influence on the final structure of the cathode, including the catalyst composition, particle size, dispersion and content. Details of the process are described below.

3.3.1 Gel preparation

$Cu_{1.25}Mn_{1.75}O_4$(CMO) gel was made from the solution precursor prepared by mixing $Cu(NO_3)_2{\cdot}2.5H_2O$ (EM Science, Germany), $Mn(NO_3)_2{\cdot}4H_2O$ (Sigma-Aldrich Co., USA), glycine (Alfa Aesar, USA), ethylene glycol (Fisher chemicals, USA) and deionized water in a mole ratio of 7: 5: 6: 6: 667. The solution was heated and held at 60°C until a highly viscous gel formed.

$La_{0.6}Sr_{0.4}Co_{0.2}Fe_{0.8}O_3$(LSCF) gel was prepared by the same procedure. $La(NO_3)_3{\cdot}6H_2O$, $Sr(NO_3)_2$, $Co(NO_3)_2{\cdot}6H_2O$, $Fe(NO_3)_3{\cdot}9H_2O$, glycine (Alfa Aesar, USA), ethylene glycol (Fisher chemicals, USA) and deionized water were mixed with the mole ratio of 6: 4: 2: 8: 10: 10: 1111.

$La_{0.8}Sr_{0.2}MnO_3$ gel was synthesized differently from the LSCF and CMO gel. $La(NO_3)_3{\cdot}6H_2O$, $Sr(NO_3)_2$ and $Mn(NO_3)_2{\cdot}4H_2O$ (Sigma-Aldrich Co., USA) were first mixed with deionized water and hold at 35°C for one hour. Citric acid and ethylene glycol were added to the solution and the temperature was raised to 60°C. The solution was held at 60°C until a highly viscous gel formed.

3.3.2 Impregnation

The impregnation of the cathode was carried out by applying a drop of the gel onto the porous YSZ matrix and holding for 6 h in air at room temperature to ensure a thorough infiltration of the gel in the porous structure. The residual gel on the surface was wiped off and the infiltrated matrix was dried in air for 12 h at room temperature before calcination. Fig. 3.5 shows that the gel infiltrated throughout the porous framework. Using gel instead of aqueous solution of metal salts helps to distribute the metal salt uniformly in the electrolyte matrix. After impregnation, the cathode was sintered at temperatures between 800°C and 1050°C to produce the catalyst particles. Two methods were employed to guarantee sufficient catalyst content in the framework, repeating the impregnation process, and increasing the concentration of the precursor gel.

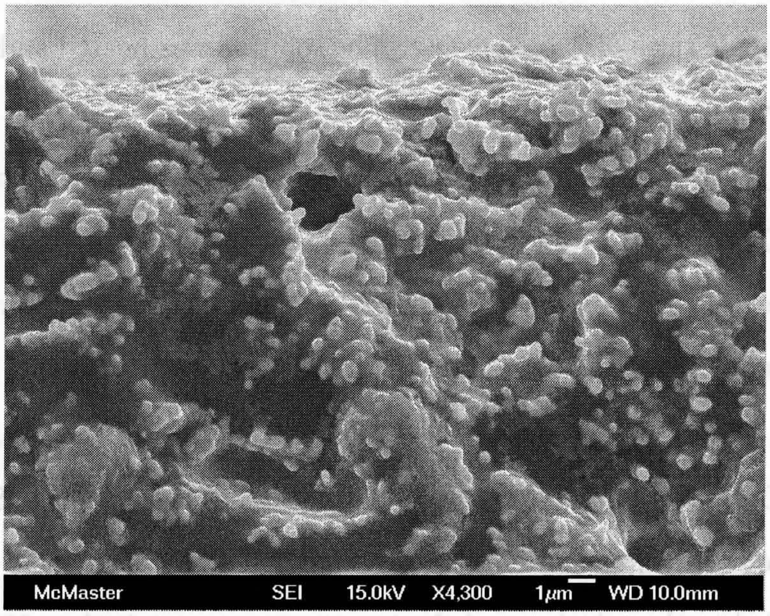

Figure 3.5: SEM image of a YSZ framework impregnated with CMO gel, after drying for 12 h in air.

3.3.3 Sintering

The sintering profile of the impregnated catalyst was designed according to the phase diagram of the catalyst oxides and the thermogravimetric analysis (TGA) results. TGA results showed that the mass change of the CMO, LSCF and LSM gel was less than 0.64% after 600°C and most of the burn-out occurred below this temperature.

As a result, in order to thoroughly burn out the polymers and NO_3^-, the cathode was first heated up to 600°C at a heating rate of 100°C/h and held at 600°C for 2 h. After that, the temperature was increased to the sintering temperature for different catalysts at a rate of 180°C/h. After holding at the sintering temperature for 2 h, the cathode was cooled to room temperature at a rate of 180°C/h. An illustration of the sintering profile is shown in Fig. 3.6.

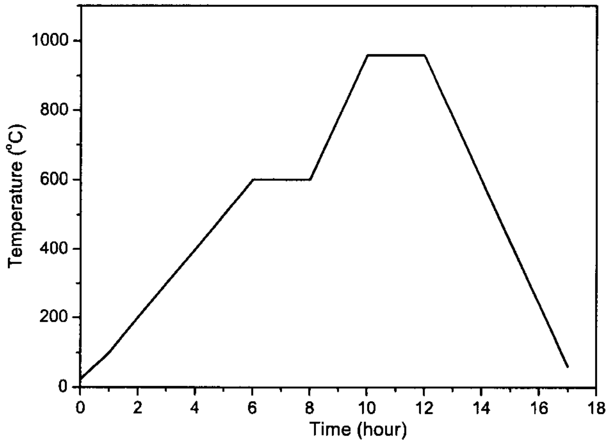

Figure 3.6: Sintering profile of the cathodes impregnated with catalyst gel.

3.4 Other components of the cell

3.4.1 Current collector layer

The current collecting layer was deposited on top of the composite layer by screen printing. $Cu_{1.25}Mn_{1.75}O_4$ ink was made by mixing $Cu_{1.25}Mn_{1.75}O_4$ powder (fabricated by Martin (2007)), 20 wt% carbon powder and screen printing oil. $La_{0.8}Sr_{0.2}MnO_3$ ink was synthesized by mixing $La_{0.8}Sr_{0.2}MnO_3$ powder, 20 wt% carbon powder and screen printing oil. A Pt current collecting layer was added in the end to enhance the contact with the Pt mesh of the test set-up.

3.4.2 Counter electrode and reference electrode

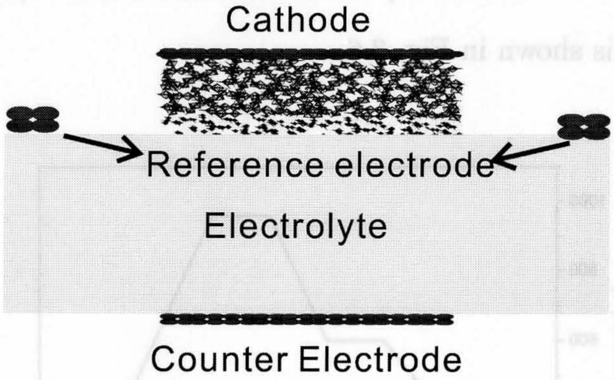

Figure 3.7: Cross-sectional schematic illustration of a fabricated cell.

The counter electrode and reference electrode were both added by screen printing Pt slurry (Engelhard, USA). The counter electrode was positioned symmetrically to the cathode while the reference electrode was deposited around the cathode at the edge of the electrolyte disc. The gap between the counter and ring reference electrodes was 4 mm. A schematic illustration of the fabricated cell is shown in Fig. 3.7.

Chapter 4

Characterization Techniques

4.1 Structural characterization approaches

4.1.1 XRD

Powder X-ray diffraction was performed using a Bruker D8 Advanced X-ray diffractometer with Cu K_α radiation ($\lambda = 1.54051$ Å), yielding information on phase composition and crystallographic parameters. Diffraction patterns were acquired for $15^\circ < 2\theta < 70^\circ$ with a scanning step and rate adjusted for the amount of powder available and the desired noise to signal ratio.

4.1.2 SEM

The microstructure of the samples was studied by scanning electron microscopy, using a JEOL JSM-7000F field emission analytical scanning electron microscope (SEM), equipped with energy dispersive x-ray spectrometry.

4.2 Electrochemical characterization methods

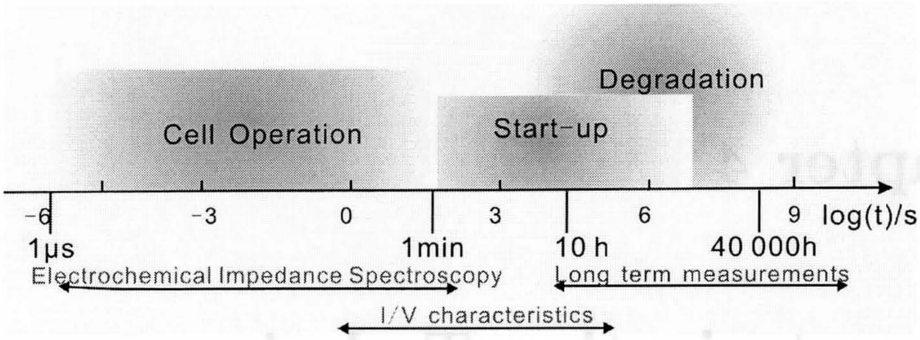

Figure 4.1: Electrochemical process response time and corresponding testing techniques. (Singhal & Kendall, 2003)

The internal physical and chemical processes of the cell determine their dynamic behaviour over a wide range of frequencies, from 1 μs to hundreds of hours (Singhal & Kendall, 2003). Electrochemical process response time and corresponding testing techniques are shown in Fig. 4.1 (Ivers-Tiffée *et al.*, 2003). In order to have a thorough understanding of the cathode-electrolyte interface behaviour and the catalytic activities of cathode materials, impedance spectroscopy, current interruption technique and cyclic voltammetry were employed to investigate the cathode's responses from 1 μs to 0.01 s. V-I measurement was carried out to study the steady state behaviour over several seconds. Long term current flow was applied to measure the cathode response in hours. The experimental methods for electrochemical measurement used in this study are detailed in the following sections. The SOFC testing arrangement used in the electrochemical measurement is shown in Fig. 4.2. A cell was fixed on top of an aluminia tube in a cylindrical furnace. Five electrode wires were connected to the cell to be used with the test equipment. Two of them were connected to the cathode, two were connected to the counter electrode and the last one was connected to the reference electrode. The electrochemical measurement was carried out without any fuel flow. In order to get a better understanding of different testing methods, an SOFC can be simplified as a circuit shown in Fig. 4.3. Both the cathode and the anode are regarded to be an RC circuit and the electrolyte functions as a series resistance.

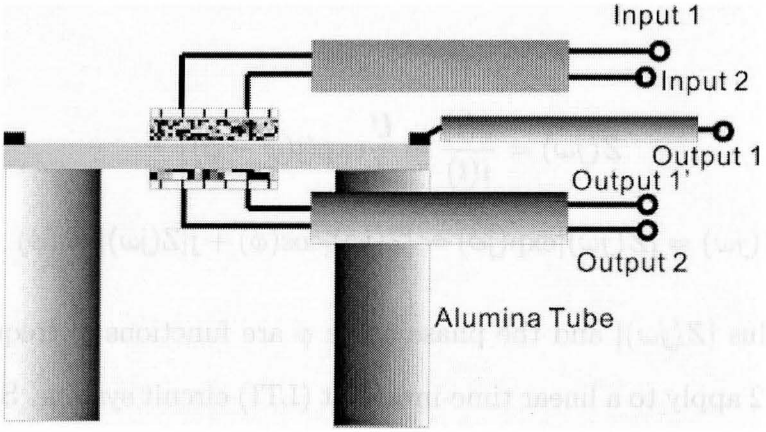

Figure 4.2: Schematic illustration of the testing set-up connection to the sample.

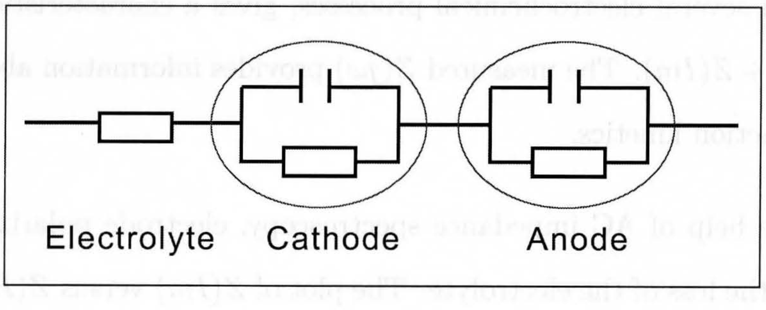

Figure 4.3: A simplified equivalent circuit model for the solid oxide fuel cell.

4.2.1 Impedance Spectroscopy

Impedance spectroscopy is a powerful technique for characterizing the electrode behavior in electrochemical systems. AC impedance is a more general type of resistance.

Its modulus and phase are dependant on the frequency. In the diagnosis of electrochemical devices such as batteries and fuel cells, impedance has become an essential concept. In the measurements, if a sinusoidal current signal, $i(t) = Icos(2\pi ft + \psi)$, is applied, a voltage response, $u(t) = Ucos(2\pi ft + \varphi)$, will be obtained. If $\omega = 2\pi f$ is defined as the angular frequency, the impedance is expressed as follows (Huang *et al.*, 2007):

$$Z(j\omega) = \frac{u(t)}{i(t)} = \frac{U}{I}\mathrm{exp}(\mathrm{j}(\varphi - \psi)) \tag{4.1}$$

$$Z(j\omega) = |Z(j\omega)|\mathrm{exp}(\mathrm{j}\phi) = |\mathrm{Z(j}\omega)|\cos(\phi) + \mathrm{j}|\mathrm{Z(j}\omega)|\sin(\phi) \tag{4.2}$$

Both the modulus $|Z(j\omega)|$ and the phase angle ϕ are functions of frequency. Equations 4.1 and 4.2 apply to a linear time-invariant (LTI) circuit system. SOFC systems can be regarded as a LTI system if the perturbation signal is small enough. When an excitation signal is imposed on a SOFC, a corresponding output signal, determined by a coupling of several electrochemical processes, gives a characteristic impedance: $Z(j\omega) = Z(R_e) + Z(Im)$. The measured $Z(j\omega)$ provides information about polarization and the reaction kinetics.

With the help of AC impedance spectroscopy, electrode polarization can be separated from the loss of the electrolyte. The plot of $Z(Im)$ versus $Z(Re)$ is called a Nyquist plot. Fig. 4.4 shows a schematic Nyquist plot for a three-electrode measurement configuration. According to the simplified equivalent circuit for the cathode in Fig. 4.3, the interface between the catalyst and the electrolyte can be regarded as an RC circuit. At very high frequency, the RC circuit is close to a short circuit, so the total resistance is equal to the resistance of the electrolyte (R_e); at very low frequency, the capacitance part of the RC circuit is close to an open circuit, so the total resistance of the circuit equals the sum of R_e and the electrode resistance (R_p). In the Nyquist plot, R_e is determined by the intercept of the real axis at high frequencies and R_p is the difference between the intercept with the real axis at low and high frequencies. In most cases, the Nyquist plot is the overlap of several semicircles and the polarization resistance is calculated by curve fitting with professional software.

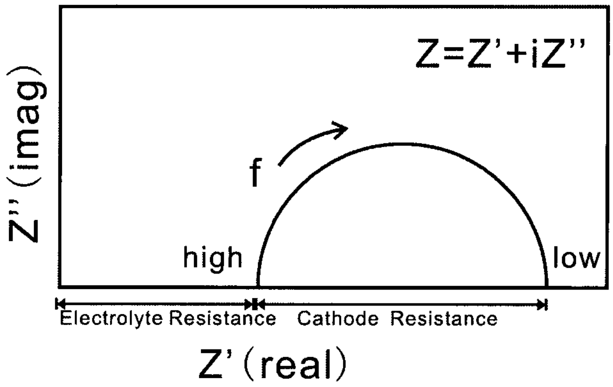

Figure 4.4: Impedance spectroscopy of an SOFC cathode.

The equipment used in this study for impedance spectroscopy measurement was a Schlumberger SI 1260 impedance analyzer. The impedance spectroscopy was measured under open circuit conditions, using an AC signal of 20 mV over a frequency range from 1.5 MHz to 0.01 Hz.

4.2.2 Current Interruption Technique

A constant current pulse of known duration was applied between both electrodes of an SOFC. Following the sudden current interruption at the end of the pulse, the voltage between both electrodes dropped back to the open circuit value, at first abruptly, then followed by an exponential tail (shown in Fig. 4.5). The vertical drop is considered to be purely ohmic and ascribed to the electrolyte resistance, whereas the exponential drop corresponds to the polarization of the electrodes. As shown in Fig. 4.3, the exponential drop of the potential reflects the potential loss of the cathode and cathode-electrolyte interface, which is called overpotential. Details on the application of the current interruption technique for the cathode overpotential measurement will be discussed in Chapter 6.

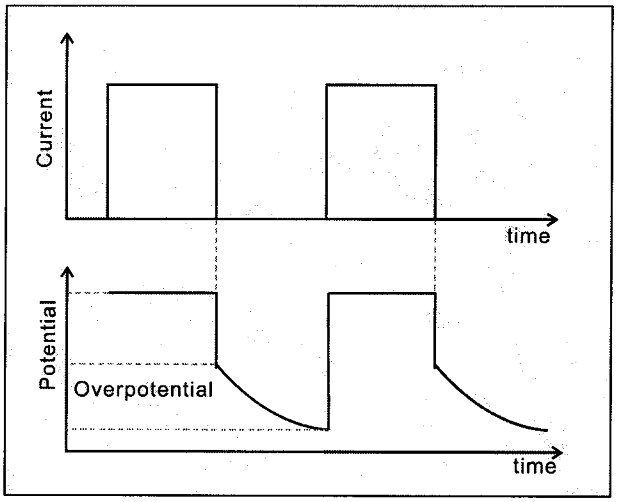

Figure 4.5: Schematic illustration of the relationship between the input interrupted current and the potential response in the overpotential measurement.

EG&G 273 potentiostat/galvanostat was employed to measure the overpotential. The data was collected by software programmed with LabVIEW 8.0.

4.2.3 Cyclic Voltammetry

Potential sweep methods are probably the most widely used among all the methods available for studying electrode processes. Two forms of the sweep experiment are linear sweep voltammetry and cyclic voltammetry, where the sweep direction is inverted at a chosen potential (Brett & Brett, 1993). A typical applied potential waveform is represented in Fig. 4.6. Upon application of a negative bias at the working electrode with respect to the counter electrode, the reduction of oxygen is driven at the working electrode - electrolyte interface, while the oxidation of oxygen ions is driven at the counter electrode - electrolyte interface, producing a cathodic current, taken as positive by convention. Current - Voltage characteristics were obtained using an EG&G 273 power source programmed through a GPIB interface using a computer interface programmed with LabVIEW 8.0.

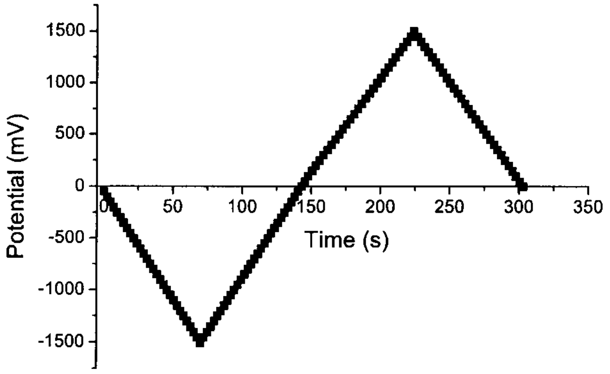

Figure 4.6: Typical potential scan applied during a cyclic voltammetry experiment.

4.3 Power Density Measurement

Power density measurements of the fabricated cells were carried out using the four-probe method. The schematic cell assembly is shown in Fig. 4.7. The test cell was sealed onto an alumina tube using Aremco-170 Ceramabond. The cell was placed inside a furnace and heated up to the testing temperature. A 7% hydrogen and Ar mixture was used as fuel for the anode and air or pure oxygen was introduced as oxidant for the cathode. The current-voltage performance of the cell was monitored by two HP multi-meters.

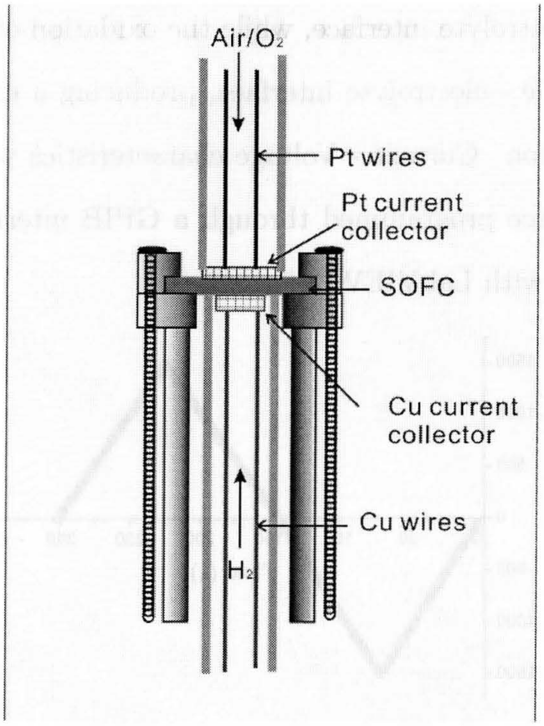

Figure 4.7: Fuel cell arrangement for power density measurement.

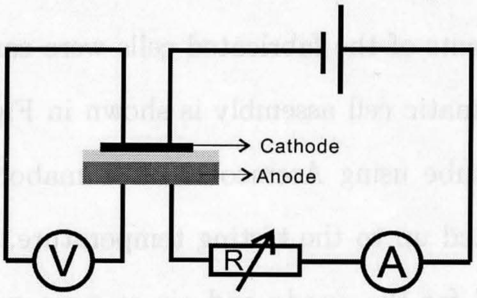

Figure 4.8: The electrical circuit for the power density measurement.

Chapter 5

Structural Characterization

5.1 Phase Analysis

Phase analysis was carried out using x-ray powder diffraction to identify the phases of the synthesized catalyst. The sintering temperature ranges were selected based on the phase diagrams of the oxides, as shown in Fig. 5.1. Sintering conditions were adjusted to obtain the desired phase of the catalyst material.

5.1.1 Copper Manganese Spinel

XRD results showed only peaks of copper manganese spinel and YSZ for both of the specimens sintered at 800°C and 850°C. The diffraction patterns are given in Fig. 5.2. All the CMO peaks labeled in the figure correspond to cubic $Cu_{1.25}Mn_{1.75}O_4$ with a lattice parameter a=8.30(5) Å. Trace amounts of Mn_2O_3 were also detected in the measurement, but its peaks are difficult to distinguish from the background in the diffraction pattern. The XRD results suggest that sintering the YSZ matrix at a higher temperature before the sintering of CMO effectively lowers the risk of reaction

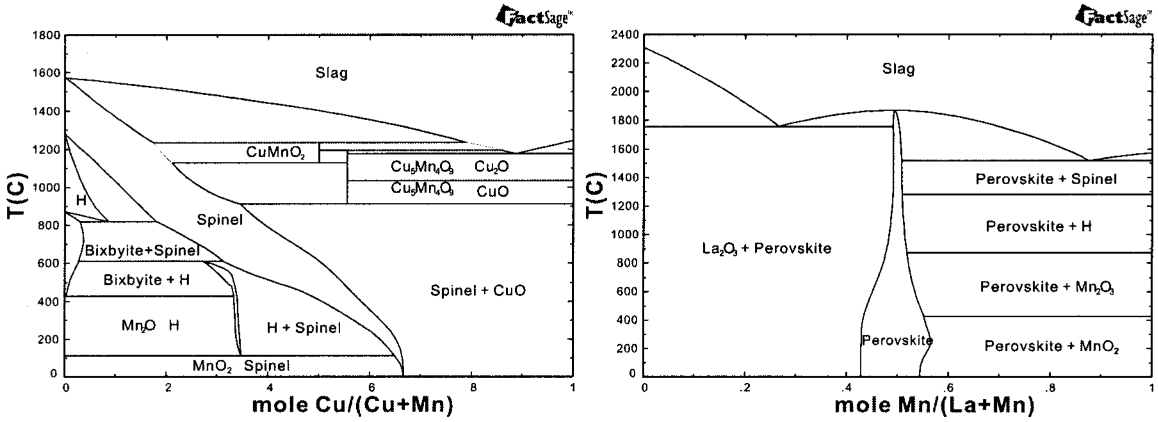

(a) (b)

Figure 5.1: (a) Tentative CuO-MnO_2 phase diagram in air at 1 atm and (b) phase diagram of the La_2O_3-Mn_2O_3 system in air.

between CMO and YSZ. CMO precursor gel of varying concentration was used to make the composite cathode. The XRD results revealed that the concentration of the gel didn't have much influence on the phase produced.

5.1.2 $La_{0.6}Sr_{0.4}Co_{0.2}Fe_{0.8}O_3$ and $La_{0.8}Sr_{0.2}MnO_3$

The XRD pattern of $La_{0.6}Sr_{0.4}Co_{0.2}Fe_{0.8}O_3$ fabricated by the impregnation method is shown in Fig. 5.3(a). The pattern was indexed in the rhombohedral perovskite system. Specimens were sintered at 850, 950 and 1050°C but only the 950°C sintered specimen had a pure $La_{0.6}Sr_{0.4}Co_{0.2}Fe_{0.8}O_3$ phase. Sintering temperature should be well controlled in this case to obtain the target phase. An XRD pattern of $La_{0.8}Sr_{0.2}MnO_3$ sintered at 850°C is also shown to be phase pure in Fig. 5.3(b). The LSM-YSZ cathode has been widely studied and is shown here for comparison to the other two electrodes.

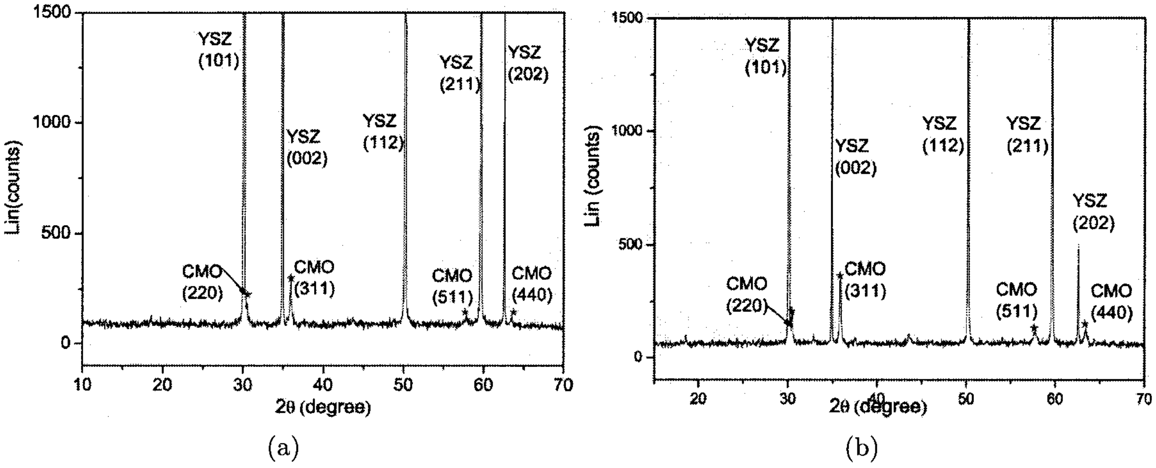

Figure 5.2: X-ray diffraction pattern of $Cu_{1.25}Mn_{1.75}O_4$ in the YSZ framework on a dense YSZ substrate. $Cu_{1.25}Mn_{1.75}O_4$ was fabricated by the impregnation method, sintered at (a) 800°C and (b) 850°C.

5.2 Microstructure

The microstructure of the entire CMO-YSZ cathode is shown in Fig. 5.4. LSCF-CGO and LSM-YSZ cathodes are composed of the same layer arrangement as CMO-YSZ. Fig. 5.4 shows that the catalyst/electrolyte composite layer, which is also called the functional layer, has much finer grain and pore structure than the current collector layer. Large pores and grains were obtained in the thick current collector layer while relatively small pores and fine-sized particles were formed in the thin composite layer. This microstructure tends to decrease the polarization loss. The cathode structure should be fine in the immediate vicinity of the electrolyte to minimize the activation polarization and coarse in the regions away from the electrolyte to minimize the concentration polarization (Singhal & Kendall, 2003).

Fig. 5.5 shows that the catalyst particles form a connected network in the electrolyte framework, which conducts electrons to the TPBs. The fine particle size of the catalyst is necessary to enlarge the TPB length in the composite layer. The pores

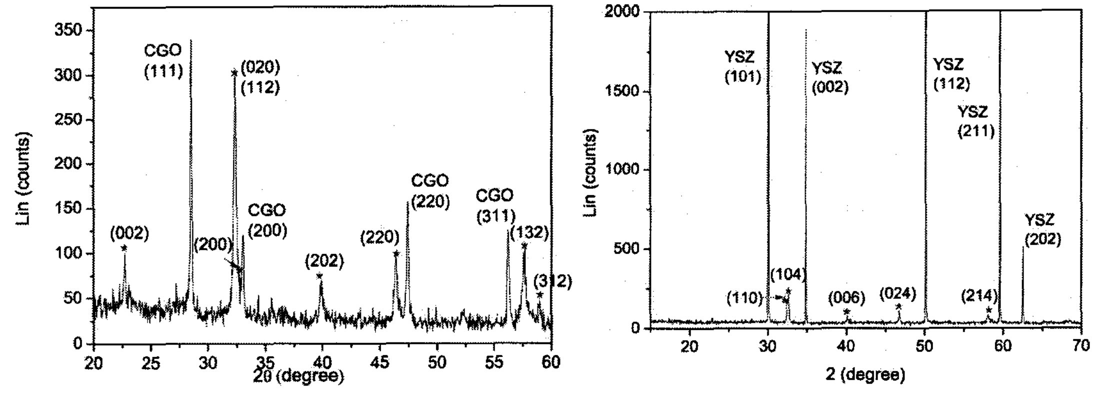

(a) (b)

Figure 5.3: X-ray diffraction patterns of (a) $La_{0.6}Sr_{0.4}Co_{0.2}Fe_{0.8}O_3$ in the CGO framework and (b) $La_{0.8}Sr_{0.2}MnO_3$ in the YSZ framework. $La_{0.6}Sr_{0.4}Co_{0.2}Fe_{0.8}O_3$ and $La_{0.8}Sr_{0.2}MnO_3$ peaks are marked out by ($\star$).

in the structure guarantee sufficient gas transport of oxygen to TPBs. The obtained microstructure is optimized for the cathode function. However, the reduced particle size will have larger resistance due to the increased number of grain boundaries. The average size of CMO particles is between 200-400 nm and under 100 nm for LSCF and LSM. The catalyst particle size was adjusted by the sintering temperature and details are discussed in Section 6.2. The density of the catalyst network can be controlled by the precursor gel concentration and the time of impregnation.

As shown in Fig. 5.5, the relative particle size of the perovskite oxides is small compared to the Cu-Mn spinel. This might be explained by the difference in melting point. The melting points of Cu-Mn spinel and $LaMnO_3$ are approximately 1200°C and 1800°C, respectively. Hence the growth of the perovskite particles is much slower than the growth of the spinel particles in the temperature range of 800 to 1000°C. The difference in sintering behavior may even be affected by the difference in the crystal structure of the two kinds of oxides: the cubic spinel structure allows cation diffusion more easily than the orthorhombic perovskite.

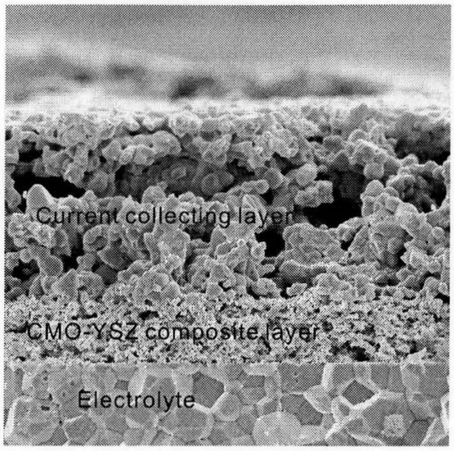

Figure 5.4: SEM image of the cross-section of a CMO-YSZ composite cathode on a YSZ dense substrate

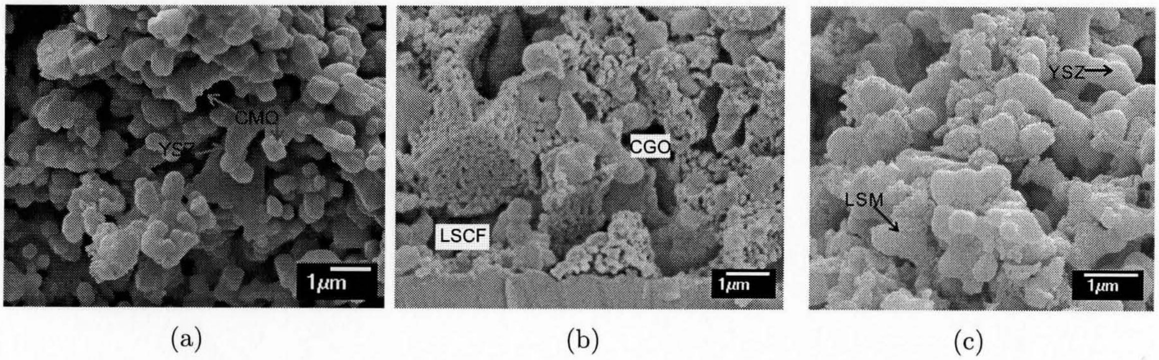

(a) (b) (c)

Figure 5.5: SEM images of the cross-section of (a) CMO impregnated YSZ functional layer, (b) LSCF impregnated CGO functional layer and (c) LSM impregnated YSZ functional layer.

Chapter 6

Polarization of the CMO-YSZ cathodes

As discussed in Section 2.6, electrode polarization is responsible for a significant portion of the large voltage loss in SOFCs. It consists of ohmic polarization, activation polarization and concentration polarization. In order to evaluate a cathode design, polarization is one of the parameters that must be considered. Polarization can be represented by polarization resistance and overpotential.

For efficient operation of an SOFC, all of these losses must be as small as possible. For the case of composite cathodes, parameters such as the electrode porosity, the pore size and the pore morphology affect the three phase boundary (TPB) length and the transport of gaseous species through the electrodes, and thus determining the activation polarization and the concentration polarization (Zhao & Virkar, 2005).

The effect of the catalyst particle size, composite layer thickness and catalyst loading on the polarization behaviour of CMO-YSZ cathodes are discussed in the following sections. Tanner's model is introduced to interpret some of the results.

6.1 Tanner's model for composite electrodes

Tanner *et al.* (1997) presented a theoretical model to assess the effect of porous, composite electrodes on the performance of SOFCs. An effective charge transfer resistance R_{ct}^{eff} was defined to describe the properties of the electrode/electrolyte interface and the microstructural parameters of the electrode. Fig.6.1 shows Tanner's analyzed electrode model, consisted of a contiguous electrolyte region, a contiguous electrocatalyst and contiguous porosity while still ensuring a long TPB length. They predicted that such an electrode might be formed by first forming a porous layer of the electrolyte material over the dense electrolyte and then infiltrating the catalyst into the pores.

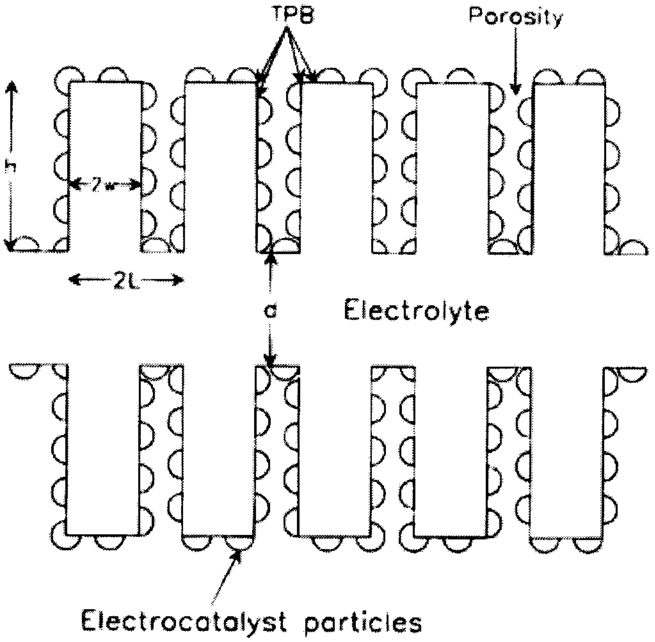

Figure 6.1: Tanner's model of a SOFC membrane with regularly spaced corrugations of the electrolyte material in the electrodes and discrete electrocatatyst particles. (Tanner *et al.*, 1997)

Tanner's model was applied with the following assumptions:

1. The catalyst region is assumed isopotential and the electronic resistance of the catalyst is negligible.
2. The oxygen ion conductivity of the electrolyte material is assumed to be independent of the position in the electrode.
3. Concentration polarization is negligible at the low current range studied.
4. The activation overpotential is ohmically related to the local current density at the catalyst-electrolyte interface.

Based on the above assumptions, the effective charge transfer resistance R_{ct}^{eff} was derived by Tanner *et al.* (1997) and yielded an analytical expression for the one-dimensional model as follows:

$$R_{ct}^{eff} = \frac{LR_{ct}}{(\frac{1+\beta}{1+\beta e^{\frac{-2h}{\alpha}}})(1-p)Le^{-h/\alpha} + (\frac{1+\beta e^{-h/\alpha}}{1+\beta e^{-2h/\alpha}})\alpha(1-e^{-h/\alpha}) + pL} \tag{6.1}$$

where

$$\alpha = [\sigma_{O^{2-}} L(1-p)R_{ct}]^{\frac{1}{2}} \tag{6.2}$$

and

$$\beta = \frac{\sigma_{O^{2-}} R_{ct} - \alpha}{\sigma_{O^{2-}} R_{ct} + \alpha} \tag{6.3}$$

R_{ct} is the intrinsic charge transfer resistance in Ωcm^2, h is the thickness of the composite electrode, $2L$ is the periodic spacing between corrugations in the electrode, p is the fractional porosity, $\sigma_{O^{2-}}$ is the oxygen ionic conductivity of the electrolyte. In the low current density regime, the dependence of overpotential on current density may be treated ohmically as $\eta = \mathrm{iR_{ct}}$. R_{ct} is related to the electrode structure by the charge transfer resistivity and certain geometric factors. Virkar *et al.* (2000) developed the numerical solution of R_{ct}:

$$R_{ct} = \frac{RT}{zFi_0} \tag{6.4}$$

in which i_0 is the exchange current density, z is the number of electrons participating in the electrode reaction, F is the Faraday constant, R is the gas constant and T is the temperature. R_{ct} is a function of the electrochemical properties of the electrocatalyst/electrolyte pair and also a function of the TPB length. i_0 can be determined experimentally for a given catalyst/electrolyte pair, and thus R_{ct} is treated as an empirical parameter.

Equation 6.1 yields an analytical expression for R_{ct}^{eff} in terms of easily measured parameters. The effect of various microstructure parameters can be evaluated by the model.

6.2 Effect of CMO particle size

As the catalyst material in the composite structure, $Cu_{1.25}Mn_{1.75}O_4$ particles play the key role in catalyzing the oxygen reduction reaction, and thus the morphology of the CMO particles should have an influence on the polarization performance of the electrodes. The dimension of the CMO particles was adjusted by varying the sintering temperature of the composite layer. Fig. 6.2 shows the microstructure of three composite cathodes prepared with ~200 nm, ~400 nm and ~500 nm CMO particles in the YSZ matrix. The weight ratio of CMO in the composite was approximately 20 wt% for all the three electrodes.

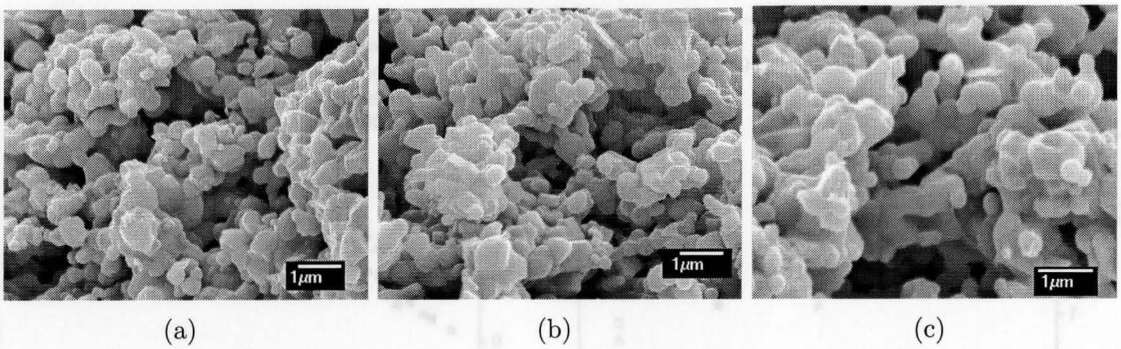

(a) (b) (c)

Figure 6.2: Microstructure of $Cu_{1.25}Mn_{1.75}O_4$-YSZ composite layers with (a) ~200 nm, (b) ~400 nm and (c) ~500 nm CMO particles.

The difference in CMO particle size was reflected in the variation of polarization resistance and overpotential of the cathodes, as shown in Fig. 6.3. The cathode with 200 nm CMO particles had the lowest polarization resistance and overpotential among the three. The R_p of cathodes with 400 and 500 nm CMO had comparable values with changing temperature. Their overpotential plots were almost overlapping at 750°C and the difference with the cathode with 200 nm CMO particle was small. The results suggest that although CMO particle size affected the polarization performance of the cathodes, the effect was not significant.

The variation of the polarization of the three cathodes stemmed from the difference in TPB length. With 20 wt% CMO in the composite layer, smaller CMO particles formed more contact points with the YSZ particles of the framework, creating a greater density of reaction sites. Since the weight ratio of CMO was relatively low, the catalyst particles covered a smaller area of the YSZ surface in the framework, and hence the effect of particle size was evident. However, Tanner's model revealed a complicated relation between the fineness of microstructure and the polarization of the electrode. In Equation 6.1, L represented the fineness of the structure and there isn't a straight-forward relation between R_{ct}^{eff} and L. This explains the reason for the

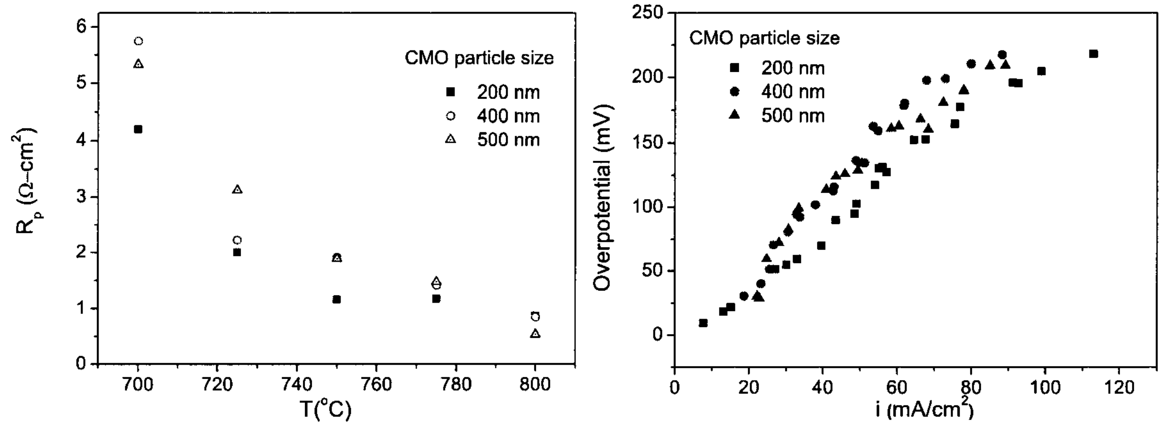

(a) (b)

Figure 6.3: (a)Polarization resistance and (b) overpotential of CMO-YSZ cathodes with various CMO particle size.

minor difference between the cathodes with 400 and 500 nm CMO particle size. The optimized particle size should be a function of oxygen partial pressure, R_{ct}, porosity and thickness of the composite layer. Under the specific experimental conditions, smaller particle size enabled decreased polarization of the electrodes.

6.3 Effect of composite layer thickness

6.3.1 Critical thickness

In the case of a two-phase mixed ionic/electronic conducting (MIEC) electrode material, the electrochemical reaction of charge transfer is spread from the electrolyte/cathode interface over some distance into the electrode. The region over which this spreading occurs depends upon the microstructure as well as the transport properties of the electrode. There is a critical thickness into the electrode, within which the current is predominantly ionic and outside which the current is mainly electronic. Thus, the cathode should exhibit mixed ionic/electronic conducting properties at least over this critical thickness (Singhal & Kendall, 2003). This layer, which is referred to as electroactive layer or functional layer, must be fine to enhance the rate of the cathodic reaction. However, the fine structure impedes gas transport, so as to increase the concentration polarization. Since there is a critical thickness, the cathode microstructure doesn't need to be fine throughout the electrode. Theoretically, developed from Tanner's model, the critical thickness λ in cm is given by Virkar *et al.* (2000):

$$\lambda = \sqrt{R_{ct} B (1 - V_v) \sigma_i} \tag{6.5}$$

in which B is the grain size of the electrolyte in the composite layer, V_v denotes the fractional porosity, σ_i denotes the ionic conductivity of the electrolyte, R_{ct} is the intrinsic charge transfer area specific resistance.

In our case, the CMO-YSZ composite layer functions as the electroactive layer, and thus its thickness must be above the critical thickness determined by the materials. Meanwhile, increased thickness of the functional layer will prevent gas transport. In order to obtain the critical thickness of the CMO-YSZ cathode, six specimens with approximately the same thickness and catalyst/electrolyte ratio were studied. From the Tafel Equation: $ln(i) = \ln(i_0) + \frac{n\alpha F\eta}{RT}$ (Equation 2.6), i_0 was extracted from the overpotential measurement results, so R_{ct} of the CMO-YSZ pair can be calculated. Fig. 6.4 shows the Tafel plots of the CMO-YSZ composite cathodes measured at 750°C. The porosity V_v of the composite layer was estimated to be approximately 50%, according to the weight change of the electrolyte pellet before and after the deposition of the composite layer. The average grain size B of the electrolyte in the composite layer was measured to be around 0.7 μm based on SEM images. The ionic conductivity of YSZ depends on the dopant content, temperature, oxygen partial pressure and the fabrication method. At 750°C and P_{O_2}= 0.2 atm, the ionic conductivity σ_i of 8%Y_2O_3 stabilized ZrO_2 was reported to be 0.02 S/cm by Van Herle *et al.* (1994). Values of the exchange current density i_0, the intrinsic charge transfer resistance R_{ct} and the critical thickness of the CMO-YSZ functional layer were calculated, as shown in Table 6.1. The average critical thickness was calculated to be 16.9±2.0 μm. It is noteworthy that the critical thickness may have a small difference within the temperature range for SOFC operation, due to the fact that i_0 is variable with changing temperature.

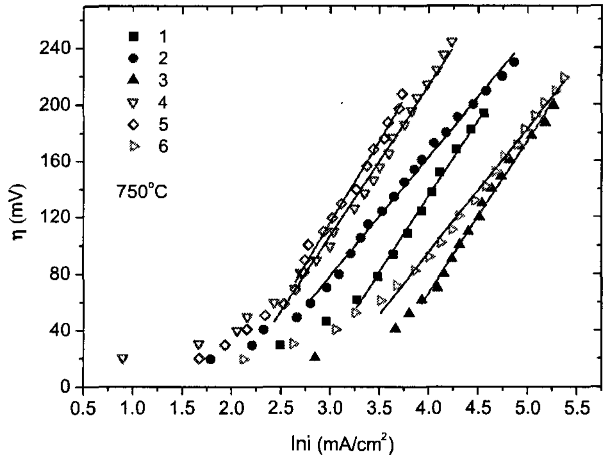

Figure 6.4: Tafel plots of six CMO-YSZ composite cathodes, measured at 750°C. The linear lines indicate the fitting of the linear parts of the plots.

Table 6.1: Critical thickness of CMO-YSZ composite cathodes.

	Sample 1	Sample 2	Sample 3	Sample 4	Sample 5	Sample 6
i_0 (mA/cm^2)	15.57	7.917	29.45	7.374	7.472	18.42
R_{ct} (Ωcm^2)	2.83	5.56	1.50	5.97	5.90	2.39
λ (μm)	14.59	20.46	10.61	21.20	21.06	13.41

6.3.2 Influence of the functional layer thickness

To further study the influence of the functional layer thickness, the polarization resistance of two batches of specimens with thickness of 13 μm and 32 μm, 10 μm and 28 μm were measured. Due to the limitation of the screen printing equipment, the minimum thickness that can be reached is ~10 μm. The thickness of the layer is controlled by several parameters during the screen printing process, including slurry fluidity, printing speed, drying time between each printing, etc. Due to the non-uniform screen printing slurry and limited accuracy of printing speed by hand operation, diligent control of the thickness was difficult to realize, and hence the variation of the sample thickness was not an integral multiple.

The result reveals that the thicker samples have higher polarization resistance than the thinner ones in the tested temperature range. 32 and 28 μm is more than the calculated critical thickness of 16.9±2.0 μm, and thus the electrodes must provide sufficient mixed ionic and electronic conducing phase. The decreased performance is probably due to the increased concentration polarization, which stemmed from the impedance of mass transport by the fine structure. Although the 10 and 13 μm samples may not provide sufficient MIEC phase for the catalytic reaction, the results suggest that samples having a thickness closer to the critical thickness had better performance. Using a composite layer with the critical thickness might be a strategy to enhance the entire cathode performance.

6.4 Effect of CMO loading

The catalyst material plays an important role in the composite layer to catalyze the oxygen reduction reaction and many studies have suggested that the content of

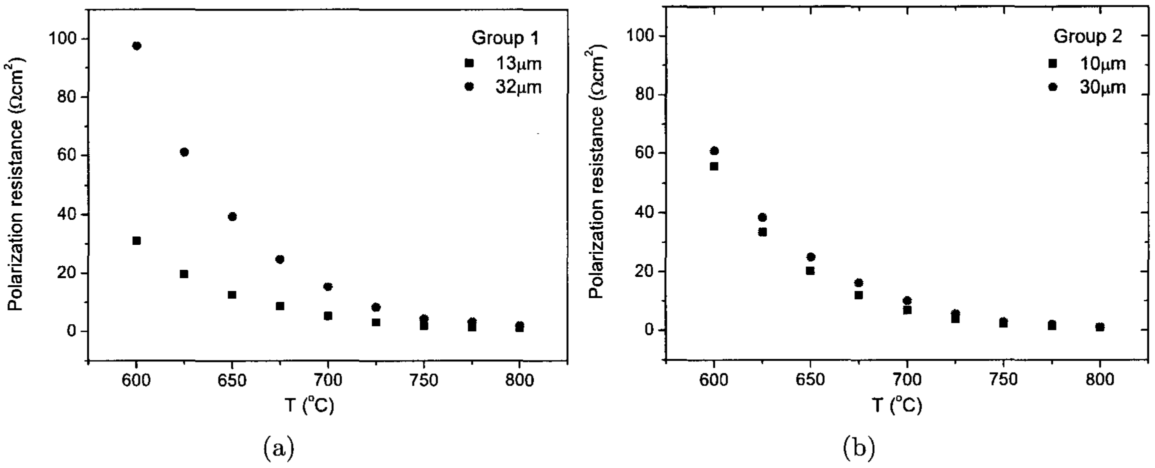

Figure 6.5: Polarization resistance of two samples of identical CMO-YSZ cathodes with various thicknesses.

the catalyst material in the composite cathode has great influence on the cathode performance. In this study, three cells with 20 wt%, 40 wt% and 50 wt% CMO impregnation were used to investigate the influence of the catalyst loading on the cathode performance. The three samples were denoted by CMO20-YSZ, CMO40-YSZ and CMO50-YSZ. For comparison with the traditional LSM material, a cell with 50 wt% LSM impregnated YSZ cathode was also fabricated with the same process, denoted as LSM50-YSZ. It may be noted that the molecular weight of the spinel and perovskite are comparable, yielding a similar catalyst content.

The polarization resistance was compared among the samples between 650 and 800°C. Fig. 6.6 shows that the polarization resistance decreased as the CMO loading increased from 20 wt% to 50 wt%. At 750°C, R_p was 1.9, 0.6, 0.3 and 8.5 Ωcm^2 for 20 wt%, 40 wt%, 50 wt% CMO and 50 wt% LSM impregnated YSZ. Although LSM50-YSZ cathode had a catalyst loading no less than the three spinel-YSZ cathodes, its polarization resistance was much higher than the spinel-YSZ cathodes in the temperature range studied. The results reveal that a loading of 40 wt% CMO in the composite layer and 750°C is recommended to achieve an acceptable polarization resistance for fuel cell operation.

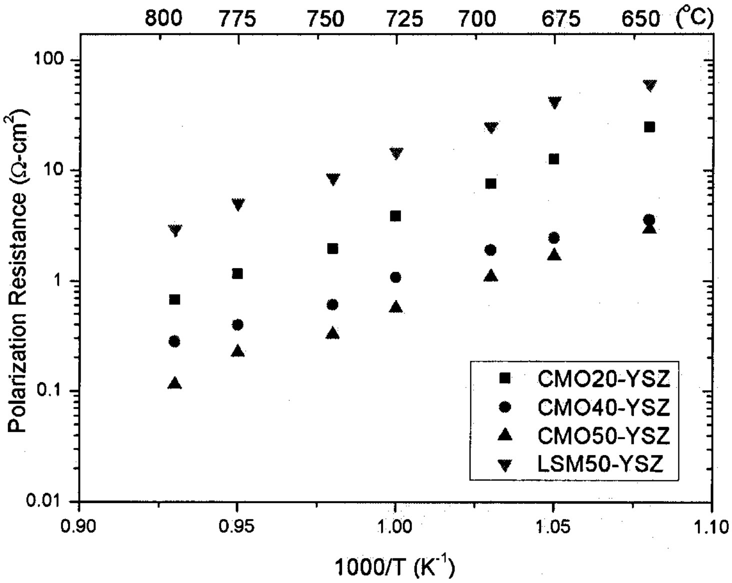

Figure 6.6: Effect of CMO loading on polarization resistance of the CMO-YSZ cathodes from 650 to 800°C, compared with LSM impregnated YSZ cathode.

The current interruption technique was employed to measure the overpotential of the cathodes at 700°C in air. LSM50-YSZ was also measured for comparison. Fig. 6.7(a) shows that the overpotential of CMO-YSZ cathodes increased with decreasing CMO content, in accord with the polarization resistance result. A deviation of the overpotential result compared with the polarization result is that LSM50-YSZ cathode has a lower overpotential than CMO20-YSZ above approximately $i_0 = 40\ mA/cm^2$, yet its polarization resistance was higher than CMO20-YSZ at 700°C as shown in Fig. 6.6. This is possibly because the continuous cathodic current supply during the measurement accelerates the catalytic ability of LSM more than CMO. The details of the cathodic current acceleration effect will be discussed in Chapter 8. However, with similar catalyst loading, spinel-YSZ cathodes still showed lower polarization loss than

LSM50-YSZ. For instance, at a current density of 100 mA/cm^2, the overpotential was 90 mV for CMO50-YSZ, 141 mV for CMO40-YSZ and 204 mV for LSM50-YSZ.

The exchange current density at the three phase boundaries, which corresponds to the oxygen reduction reaction rate, was subtracted from the Tafel plots in Fig. 6.7(b). At 700°C, the exchange current density for CMO20-YSZ, CMO40-YSZ and CMO50-YSZ was 7.78, 19.36 and 37.81 mA/cm^2, respectively. By comparison, LSM50-YSZ had an exchange current density of 3.38 mA/cm^2, which was even lower than that of the 20 wt% CMO impregnated YSZ cathode. The result indicates that the reaction rate of the CMO-YSZ cathode is approximately ten times faster than the LSM-YSZ cathode with the same amount of catalyst material.

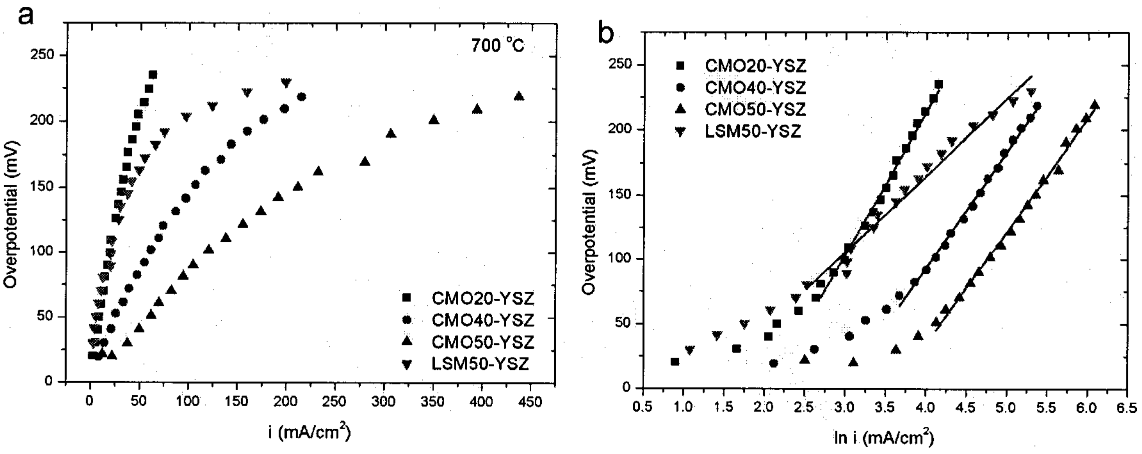

Figure 6.7: (a) Overpotential curves and (b) Tafel plots of CMO-YSZ cathodes at 700°C with varying CMO loading, compared with LSM50-YSZ under the same conditions.

Based on the discussion above, the CMO content in the composite cathode is also shown to have a great influence on the cathode performance. This can be explained by Tanner's model. Virkar *et al.* (2000) reported that R_{ct}^{eff} achieved an asymptotic value with an increasing electrode thickness. Recall Equation 6.1, as

$h \rightarrow \infty$, R_{ct}^{eff} is given by (Tanner *et al.*, 1997):

$$R_{ct}^{eff} \approx \sqrt{\frac{BR_{ct}}{\sigma_i(1-V_v)}} \tag{6.6}$$

As discussed in section 6.3, the thickness of the composite layer used is close to or greater than the critical thickness, and hence Equation 6.6 may be used to give a rough estimate of the loading effect. The electrolyte grain size B and ionic conductivity σ_i are regarded as constants. Increasing the loading of CMO in the composite layer has two effects. First, it lowers the exchange current density i_0, which in turn decreases R_{ct}, according to Equation 6.4. Second, the increased amount of catalyst particles in the framework decreases the porosity of the functional layer. Smaller values of R_{ct} and V_v both favour the lowering of R_{ct}^{eff}. Since R_{ct}^{eff} is the effective charge transfer resistance, the lower value of R_{ct}^{eff} indicates decreased polarization losses. It is also possible to predict that, if the loading of CMO exceeds a critical value, at which the porosity V_v is too low, the concentration polarization governs the total polarization loss, and the polarization resistance and overpotential of the cathode would increase with CMO loading. The study of the threshold ratio of CMO on the cathode performance at different temperatures is an avenue for future work.

In general, with increasing CMO content in the YSZ matrix, the length of the triple phase boundary is extended and the network of the electronic conductive phase is better connected, leading to a lower polarization at 50 wt% impregnation of CMO. Meanwhile, the decreased polarization loss of CMO50-YSZ compared with LSM50-YSZ shows that CMO is an effective catalyst for the oxygen reduction reaction.

6.5 V-i performance

Anode supported cells were fabricated to study the voltage-current relationship of the cells with the CMO-YSZ and LSM-YSZ cathodes. The power output of the cell was calculated according to measured V-i values. The anode supported half cells were provided by Versa Power Systems Ltd. The half cell was composed of a thick Ni-YSZ cermet anode with a thickness of ~0.5 mm and a ~10 μm thick YSZ electrolyte layer. CMO-YSZ and LSM-YSZ composite cathodes were added on top of the YSZ film using the same procedure as for the home-made electrolyte pellets. The reason to use the anode supported cell was to eliminate the loss of the cell contributed by the thick electrolyte, and hence the cathode became the key part affecting the performance of the cell.

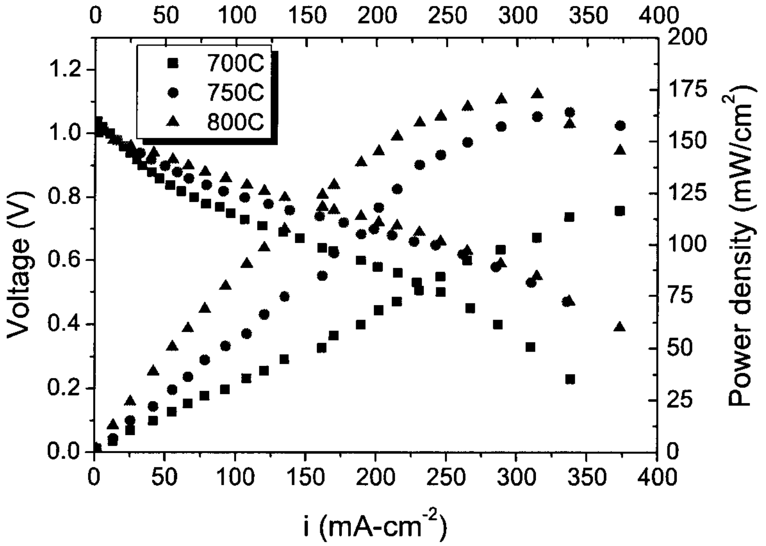

Figure 6.8: Voltage-current relation and power density of the CMO-YSZ cathodes at 700, 750 and 800°C, with 7%H_2-Ar mixture fed to the anode and pure O_2 fed to the cathode.

Fig. 6.8 shows the voltage-current relationship and power density of a cell with 40 wt% CMO impregnated YSZ cathode at 700, 750 and 800°C, with 7%H_2-Ar mixture fed to the anode and pure O_2 fed to the cathode. The open circuit voltage (OCV) of the cell at three temperatures were all ~1 V, indicating the sealing of the cell to the testing set-up was acceptable. The value of output voltage was almost equal at 750 and 800°C, both higher than at 700 °C. The peak power densities were 123, 165, 172 mW/cm^2 at 700, 750 and 800°C.

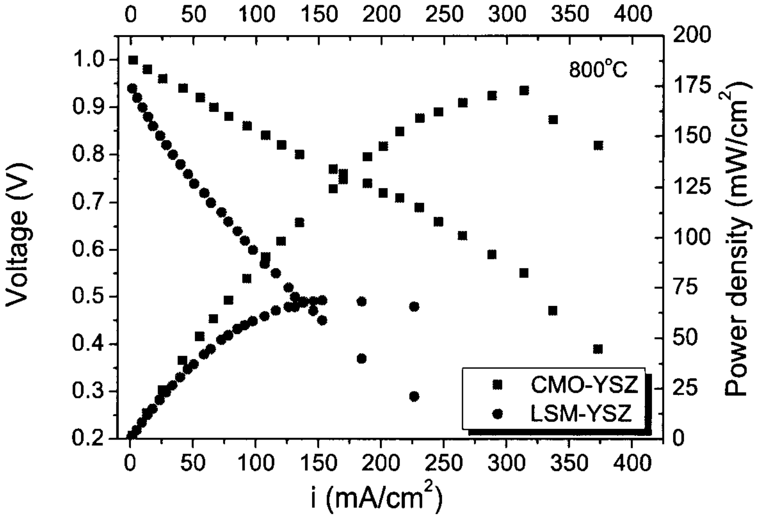

Figure 6.9: Voltage-current relation and power density of the CMO-YSZ and LSM-YSZ cathodes at 800°C, with 7%H_2-Ar mixture fed to the anode and pure O_2 fed to the cathode.

A cell using an LSM-YSZ composite cathode with 40 wt% LSM impregnation was tested under the same conditions. Fig. 6.9 shows the V-i behaviour of the LSM-YSZ and CMO-YSZ cells measured at 800°C. The output voltage drop was much sharper for the LSM-YSZ cell than for the CMO-YSZ cell. The peak power density of the CMO-YSZ cell was approximately 2.5 times higher than the LSM-YSZ.

The V-i relationship reveals good consistency with the results discussed in Section 6.4. The polarization of CMO-YSZ cathodes decreased with increasing temperature and increased power density at higher temperatures was observed in the V-i measurements. CMO-YSZ cathodes revealed lower polarization than LSM-YSZ cathodes with the same catalyst content, and thus higher power density was achieved by the cell with the CMO-YSZ cathode compared to the one with the LSM-YSZ cathode at the same temperature.

There are several aspects of the set-up that can be optimized to increase the power density of SOFCs. Sealing of the cell was believed to have great influence on the cell efficiency but various extents of leaking were always detected in our system. Increased power density was generally obtained by using humidified hydrogen gas as fuel, instead of 7%H_2-Ar mixture. Moreover, the contact between the current collector meshes and the electrodes introduced considerable contact resistance, which contributed to the cell resistance in the V-i measurement. Better contact between the mesh and the electrode is expected to decrease the internal loss.

Chapter 7

Cathodic Reaction Mechanism

As discussed in Section 2.5, the cathode reaction includes several processes: gas diffusion, adsorption and dissociation of oxygen, diffusion of adsorbed oxygen, diffusion of dissolved oxygen in the electrolyte and charge transfer across the electrode/electrolyte interface (Minh, 1995). The main concern of the reaction mechanism study is to find out the rate determining processes of the cathode reaction.

7.1 Rate determining processes

Impedance spectroscopy is a powerful technique for characterizing the electrode behaviour in electrochemical systems. AC impedance spectroscopy is employed to obtain an understanding of the oxygen reduction reaction mechanism in the CMO-YSZ and LSCF-CGO composite cathodes.

The equivalent circuit model (ECM) for impedance spectroscopy is easily understood, and hence it has been used extensively in SOFC performance diagnosis. Idealized equivalent circuit models are often constructed to simulate the physical and chemical processes taking place in SOFC systems. Each discrete circuit element of an ECM has corresponding physical and chemical analogies, such as mass-transfer, charge transfer, electrolyte resistance, and electrochemical reaction conductance. The elements used in the ECM to simulate the cathode process in our study include resistors and constant phase elements (CPE). A constant phase element is not a real electrical component but defined by its mathematical function. Often a CPE is used in a model in place of a capacitor to compensate for non-homogeneity in the system.

7.1.1 Literature survey

Various authors have investigated the oxygen reduction reaction in LSM or LSM/YSZ composite electrodes and found different numbers of rate limiting processes. CMO has the same Mn^{3+}/Mn^{4+} redox couple as LSM while LSCF has the same perovskite structure as LSM, and therefore the results obtained for LSM and LSM-YSZ composite cathodes are helpful to reveal the oxygen reduction mechanism for the CMO-YSZ and LSCF-CGO systems.

For the simplest case, a point LSM electrode in contact with YSZ was studied by Siebert *et al.* (1995). In this system, the oxygen reduction reaction was found to be mainly limited by one process, having an activation energy of 1.8 eV. LSM cone cathodes in contact with YSZ were reported to have two limiting processes during the cathode reaction by Skou & Jacobsen (1989) and Odgaard & Skou (1996). Charge transfer and mass transfer processes were assumed to correspond to the high frequency and low frequency arcs in the impedance spectra, respectively. Youngblood *et al.* (1993) studied a roughened LSM cathode with a roughened YSZ surface system. Charge transfer was also suggested as the corresponding process at high frequency, while oxygen dissociation was indicated to dominate the low frequency regime.

A more complicated situation is the LSM porous cathode on a YSZ electrolyte. Various numbers of arcs have been found in the impedance spectra by different authors. Murray *et al.* (1998) identified one arc having an activation of 1.6 eV and a characteristic frequency of 3-4 kHz at 850°C in air. Oxygen dissociation and adsorption on the electrode were regarded as the corresponding processes. Østergård & Mogensen (1993) investigated the rate limiting steps for $La_{0.85}Sr_{0.15}MnO_3$ cathodes at 1000°C. The high frequency arc was tentatively suggested to be charge transfer of oxygen ions from the cathode/electrolyte interface to vacancies in the YSZ electrolyte. The medium frequency process was ascribed to dissociation of adsorbed oxygen molecules. The low frequency arc possibly represented the diffusion of oxygen ions to the cathode/electrolyte interface.

When an LSM-YSZ composite cathode was used, the impedance became even more complex. Geometric effects of the microstructure were reflected in the impedance spectra, which provided more information about the reaction mechanism. Juhl *et al.* (1996) found two rate limiting processes for the $(La_{0.75}Sr_{0.25})_{0.9}MnO_3$-YSZ composite cathode between 700 and 1000°C. The low frequency process was ascribed to a chemical elementary process in the overall oxygen reduction, based on decreasing resistance of this process with increasing composite thickness. The high frequency process was attributed to transport phenomena in the composite layer. Murray *et al.* (1998) found a high frequency arc in the LSM/YSZ composite cathode, in addition to the arcs found for porous LSM electrodes. The high frequency contribution was ascribed to YSZ grain boundary resistance in the composite cathode. Kim *et al.* (2001) reported three arcs in the impedance spectra of the LSM-YSZ composite cathodes. The high-frequency arc was attributed to oxygen ion transfer from the three-phase boundary to the electrolyte. The intermediate-frequency arc was ascribed to oxygen ion surface diffusion. The low-frequency arc was related to gas phase diffusion.

The investigation of LSM and LSM-YSZ composite cathodes showed that impedance spectroscopy strongly depended on the nature of the electrode. Various processes may be rate limiting, depending on the electrode microstructure, composition, processing parameters and measurement conditions.

7.1.2 CMO-YSZ cathode

The impedance data of CMO-YSZ cathodes generally included a high frequency tail ascribed to the measurement leads and one to three processes contributing to the electrode impedance spectrum. The number of processes and the magnitude of each contribution varied with the cathode composition, the fabrication process and the test conditions. Fig. 7.1 shows an example of the variations of the arcs in the impedance spectra of three CMO-YSZ composite cathodes with different CMO content at the same temperature. The characteristic frequency for each arc is labeled in the spectra. Each arc in the spectrum may be the overlap of several arcs and represent one or more processes.

Fig. 7.2 shows impedance spectroscopy measured for the CMO50-YSZ cathode between 600 and 775°C. Two visible arcs were observed in the spectra below 725°C and the arcs started to merge after 725°C. The spectra were analyzed by using the equivalent circuit models shown in Fig. 7.3. In the equivalent circuit model, (R_2-CPE1) and (R_4-CPE2) represent the processes related to the high-frequency and low-frequency arcs, respectively. R_1 represents the resistance from the electrolyte, R_2 represents the polarization resistance of the high frequency process, R_4 represents the polarization resistance of the low frequency process, and CPE1 and CPE2 are constant phase elements for the two processes. Fig. 7.3 shows the fitting curve and the

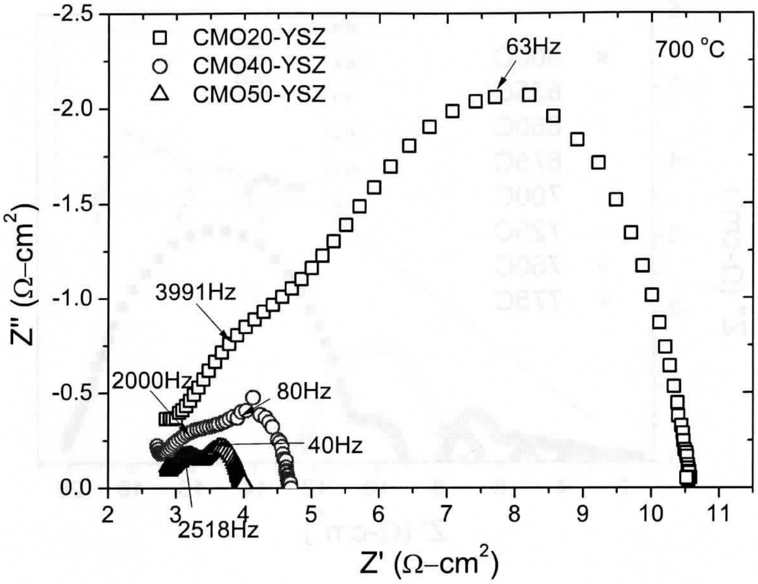

Figure 7.1: Impedance spectroscopy of the CMO-YSZ cathodes at 700°C. The characteristic frequency is labeled for each arc.

experimental results are in good agreement. The values of the electrical elements and the characteristic frequency of each arc are listed in Table 7.1. From 600 to 750°C, R_4 showed a much more obvious decrease than R_2, which indicates that increasing temperature had a stronger effect in accelerating the process related to the low frequency arc than the high frequency arc. The size of the two arcs both decreased with increasing CMO content in the composite layer, as shown in Fig. 7.1.

Table 7.1: Equivalent circuit elements for impedance spectroscopy of the CMO50-YSZ composite cathode.

T (°C)	R_1 (Ωcm^2)	R_2 (Ωcm^2)	f_{high} (Hz)	R_4 (Ωcm^2)	f_{low} (Hz)
600	9.04	1.65	1261	9.34	3.17
650	4.84	1.02	2000	2.04	10
700	2.78	0.77	2517	0.43	39.9
775	1.46	0.27	1588	–	–

The frequency range for the high frequency arcs in Fig. 7.3 was between 10^5

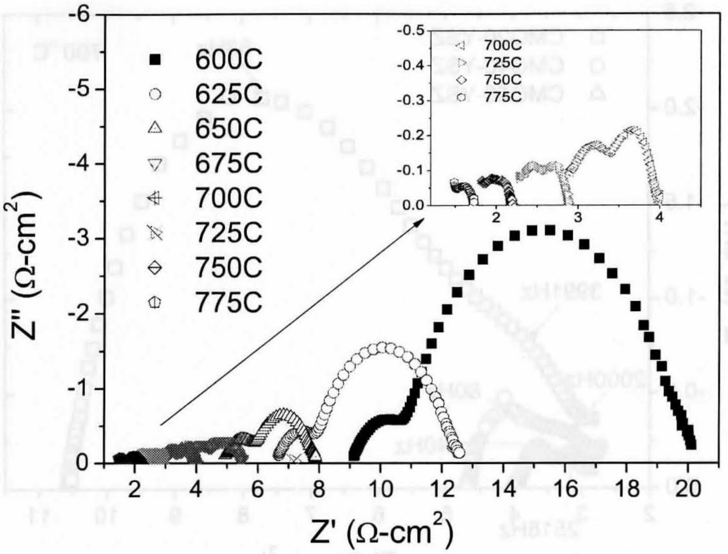

Figure 7.2: Impedance spectroscopy of the CMO50-YSZ cathode between 600 and 775°C.

and 317 Hz. It is possibly an overlap of the high and intermediate frequency arcs referred by Kim *et al.* (2001), and thus the high frequency arc of CMO-YSZ composite cathodes is associated with processes including oxide ion diffusion in the bulk and surface of the cathode and incorporation of oxygen ions from the three-phase boundary into the YSZ lattice. The low frequency arc represents the mass transfer process, which includes adsorption and desorption of oxygen, oxygen diffusion at the gas and film interface. Fig. 7.3(d) shows that the high frequency arc governed the entire spectrum at 775°C, in which the low frequency arc almost vanished.

7.1.3 LSCF-CGO cathode

The composite cathode consisting $La_{0.6}Sr_{0.4}Co_{0.2}Fe_{0.8}O_3$ and CGO fabricated by the impregnation method was studied by impedance spectroscopy to explore the oxygen reduction reaction mechanism. One or two arcs appeared in the spectra, depending

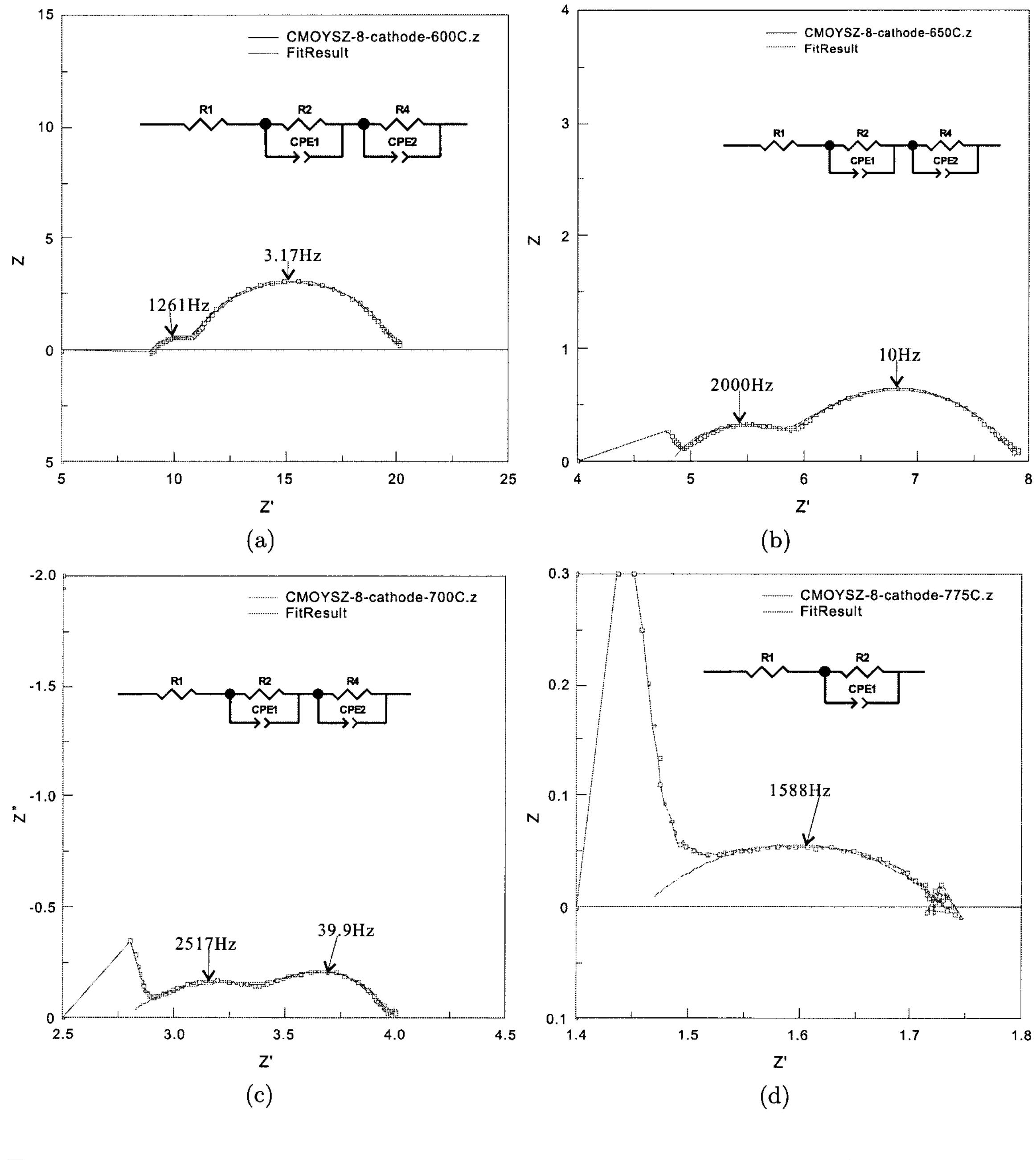

(a) (b) (c) (d)

Figure 7.3: Impedance spectroscopy of a CMO40-YSZ cathode at (a)600, (b) 650, (c) 700 and (d) 775°C. The solid line shows the fitting result of the equivalent circuit model shown in each graph.

on the different fabrication and measurement conditions.

Fig. 7.4 shows the impedance spectra of LSCF-CGO cathode sintered at 950°C. The two separable impedance arcs observed at low and high frequencies reveal that the oxygen reduction reaction was limited by at least two cathode processes, similar to CMO-YSZ cathodes. The impedance spectra of the LSCF-CGO composite cathode can also be described by the equivalent circuit model shown in Fig. 7.5. R_c and R_m represent the resistance of the high and low frequency processes, respectively. The variation of R_c and R_m with increasing temperature is given in Table 7.2. At high temperatures (e.g., from 750 to 800°C), the effect of R_c was difficult to detect in the EC model as the value became close to zero. The low frequency arc dominated the impedance spectra from 600 to 750°C. The characteristic frequencies of the low frequency process increased from 8 to 251.8 Hz with increasing temperature. The size of the low frequency arc decreased rapidly from 600 to 675°C, but had a minor change from 700 to 800°C. Neither the characteristic frequency nor the size of the high frequency arc had significant changes with varying temperature.

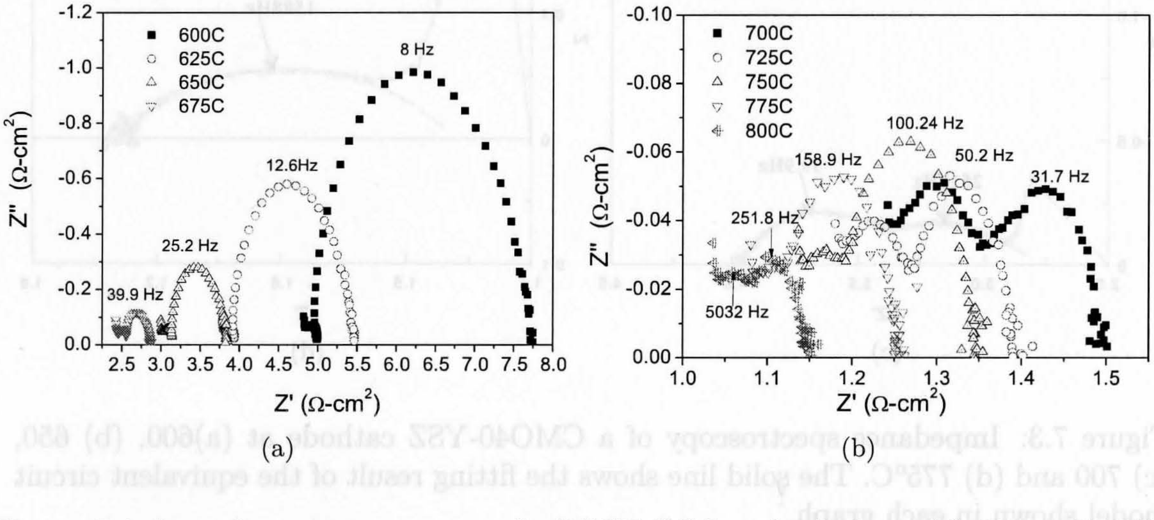

(a) (b)

Figure 7.4: Impedance spectroscopy of a LSCF-CGO cathode from (a) 600 to 675°C and (b) 700 to 800°C.

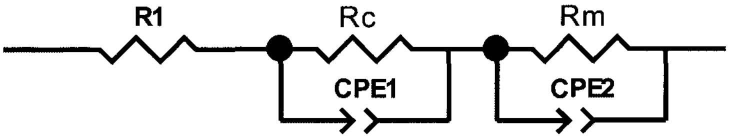

Figure 7.5: Equivalent circuit model for LSCF-CGO cathode.

Table 7.2: Equivalent circuit element for LSCF-CGO composite cathode.

T (°C)	600	625	650	675	700	725	750	775	800
R_c (Ωcm^2)	0.213	0.202	0.1968	0.189	0.1826	0.140	~0	~0	~0
R_m (Ωcm^2)	2.904	1.605	0.7574	0.338	0.153	0.138	0.1658	0.1474	0.086

In the case of a mixed ionic electronic conducting electrode, according to Jerdal (1998), the low frequency arc was due to a slow redox reaction at the surface of the electrode. The medium frequency arc was due to diffusion of oxide anions in the bulk of the electrode. The high frequency arc was related to oxygen vacancy exchange at the electrode/electrolyte interface. Hansen & Vels Hansen (2007) studied the $(La_{0.6}Sr_{0.4})_{1-s}Fe_{0.8}Co_{0.2}O_{3-\delta}$ cathode and reported that the high and medium frequency arcs were cobbled and depended on the same property of the electrode material. It's difficult to decide the specific process for each arc just from the temperature dependance and further experiments are required to obtain a clear understanding of the cathode reaction mechanism in LSCF-CGO composite cathodes.

7.2 Activation energy

7.2.1 Arrhenius equation

Activation energy (E_a) is a fundamental parameter that characterizes the cathode reaction. It's different from polarization, which is a combined result of several factors, such as cathode reaction, TPB length, gas flow, etc. Activation energy can be used to analyze the specific process involved in the entire cathode reaction. Activation energies of the cathode reactions are derived from the Arrhenius equation:

$$\sigma = (A_0/T)\exp(-E_a/kT) \tag{7.1}$$

where σ is the conductivity, A_0 is the pre-exponential factor, T is the absolute temperature, E_a is the activation energy, and k is the Boltzmann constant. Taking the natural logarithm of the Arrhenius equation yields:

$$ln(\sigma T) = lnA_0 - (E_a/k)\frac{1}{T} \tag{7.2}$$

When a reaction obeys the Arrhenius equation, a plot of $ln(\sigma T)$ versus $\frac{1}{T}$ gives a straight line, whose slope and intercept can be used to determine E_a and A_0. By deriving the $ln(\sigma T)$ versus $\frac{1}{T}$ for the different processes discussed in Section 7.1.2 and 7.1.3, the activation energy of the entire cathode reaction and the process related to the specific arc in the impedance spectra can be calculated.

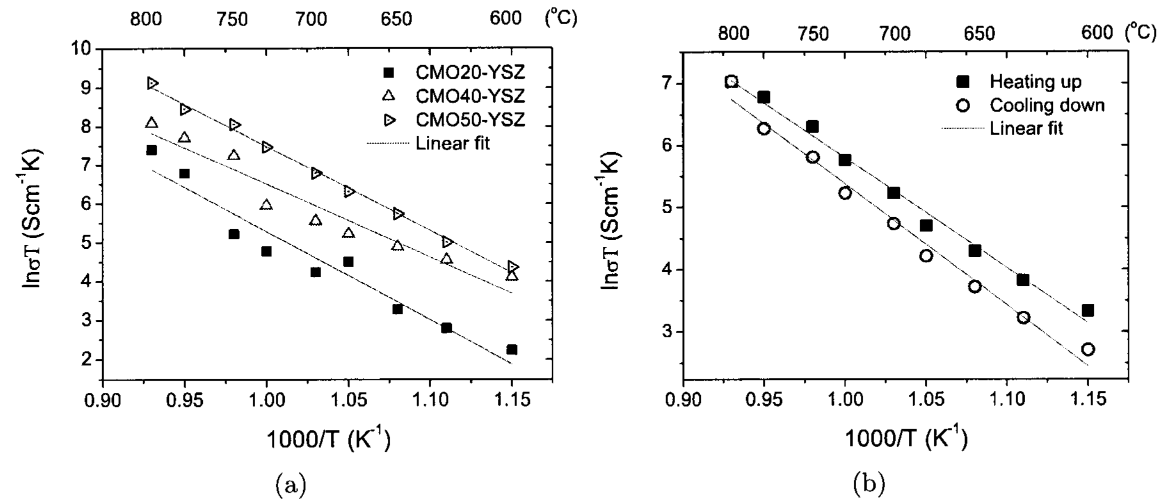

Figure 7.6: Arrhenius plots of (a) CMO-YSZ composite cathodes with various CMO loadings in the composite layer and (b) a CMO20-YSZ cathode at different stages in a thermal cycle.

7.2.2 E_a of CMO-YSZ composite cathodes

Equation 7.2 was employed to estimate the activation energy of the cathode reaction at CMO-YSZ composite cathodes. Fig. 7.6(a) shows the relation between $ln(\sigma T)$ and $\frac{1}{T}$ of CMO-YSZ composite cathodes between 600 and 800°C. The three cathodes examined were impregnated with 20wt%, 40wt% and 50wt% CMO, denoted as CMO20-YSZ, CMO40-YSZ and CMO50-YSZ. E_a values calculated from the slopes of the plots are 1.96, 1.62, and 1.88 eV for CMO20-YSZ, CMO40-YSZ and CMO50-YSZ. As discussed in Section 6.4, CMO50-YSZ had the lowest polarization resistance and highest exchange current density among the three electrodes, but its activation energy was higher than CMO40-YSZ. Although the energy barrier for the oxygen reduction reaction was lower for CMO40-YSZ compared with CMO50-YSZ, the longer TPB length of CMO50-YSZ caused it to have better cathode performance. The results demonstrate that the activity of a cathode was influenced by both its microstructure and material property. Fig. 7.6(b) reveals the effect of SOFC operation thermal cycle on the activation energy of the CMO-YSZ cathode. A CMO20-YSZ cell was first heated up from 600 to 800°C and then cooled down from 800 to 600°C. E_a is calculated to be 1.53 eV for the heating up process and 1.68 eV for the cooling down process. The results suggest that heating to 800°C affected the microstructure of the cathodes and caused the variation in the activation energy. The thermal cycle (i.e., time spent at each temperature) in the measurements was not ideally identical due to different testing conditions. The deviation of the data points of CMO20-YSZ and CMO40-YSZ in Fig. 7.6(a) may be because of the influence from the thermal cycle.

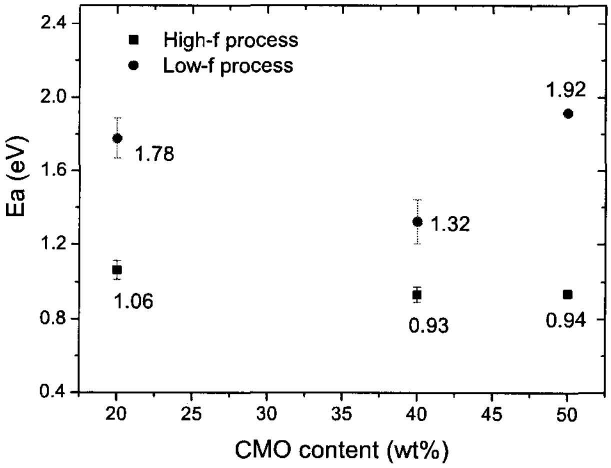

Figure 7.7: E_a of the high and low frequency processes in CMO-YSZ composite cathodes between 600 and 800°C.

The activation energy of the high and low frequency processes of CMO-YSZ composite cathodes (Fig. 7.1) was calculated as well. Fig. 7.7 shows E_a of cathodes with three CMO loadings in the composite layer between 600 and 800°C. Impedance spectroscopy of several specimens having 20 wt% and 40 wt% CMO impregnation and only one with 50 wt% impregnation were measured, and hence there is no error bar for the 50 wt% data in Fig. 7.7. Jørgensen & Mogensen (2001) summarized

Table 7.3: Overview of the activation energy and processes affecting the impedance of LSM/YSZ composite cathodes. (Jørgensen & Mogensen, 2001)

Arc	$f_{max}(Hz)$	$E_a(eV)$	Process
A	$\sim 10^4, 5 \times 10^3$	1	Transport/transfer of oxygen intermediates/oxide ions between LSM and YSZ and through the YSZ of the composite.
B	$10^2 - 5 \times 10^3$	N/A	Reflects competitive elementary processes in the overall oxygen reaction mechanism.
C	$0.1 - 10^4$	2, 1.8-1.9, 1.5-1.6	The processes are assumed to be dissociative adsorption, transfer of species at TPB and surface diffusion.

the activation energy and processes affecting the impedance of LSM/YSZ composite cathodes from several studies, given in Table 7.3. As discussed by Juhl *et al.* (1996), Kim *et al.* (2001), Murray & Barnett (2001) and Jørgensen & Mogensen (2001), the high frequency process may relate to the charge transfer, diffusion process or both. As shown in Table 7.3, Murray & Barnett (2001) reported that the activation energy of this process was 1 eV. Fig. 7.7 revealed that E_a of the high frequency process was close to 1 eV and didn't vary significantly with CMO content, indicating that it was not sensitive to the TPB length. Although the high frequency process in our study should be the overlap of the charge transfer and oxygen ion diffusion, since charge transfer between the catalyst and the electrolyte is sensitive to the TPB length, it's the oxygen ion surface diffusion that dominated the high frequency process. The activation energy of the low frequency process was higher than the high frequency process and didn't show an obvious relation with different CMO content. E_a of the low frequency process was between 1.32 and 1.92 eV and the characteristic frequency ranged from 3 to 1500 Hz.

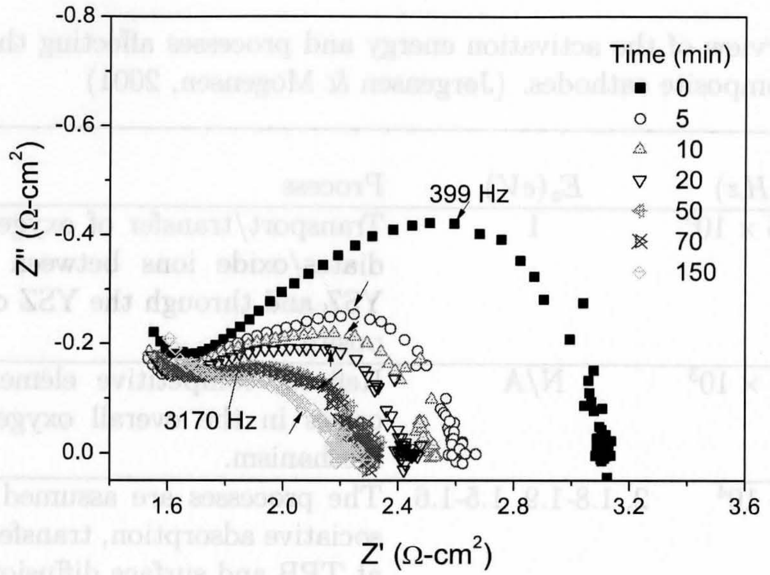

Figure 7.8: Variation of impedance spectroscopy of CMO-YSZ composite cathodes with cathodic current passage at 800°C. The black arrows indicate the point corresponding to 399 Hz, which is the characteristic frequency of the low frequency arc.

In order to further identify the cathode reaction processes corresponding to the low frequency arc, the variation of the impedance spectra of a CMO20-YSZ composite cathode was recorded with cathodic current passage time. The cathodic current had an activation effect on the CMO-YSZ composite cathodes, the details of which are discussed in Section 7.4. Fig. 7.8 reveals that the low frequency arc was sensitive to cathodic current and the size of the arc decreased with increasing time of the current passage. The size of the low frequency arc also showed obvious decrease with increasing temperature as discussed in Section 7.1.2. Jørgensen & Mogensen (2001) reported that the magnitude of arc B in Table 7.3 changed with current passage. Its E_a was between 1.5 and 2 eV and the characteristic frequency ranged between 0.1 and 10000 Hz. The processes were assumed to be dissociative adsorption, transfer of species at the TPB and surface diffusion. Since the high frequency arc has been ascribed to surface diffusion, it's reasonable to assume that the low frequency process in CMO-YSZ composite cathodes represents mass transfer reactions, including dissociative adsorption and transfer of species. However, surface diffusion still influences the low frequency process, especially when the characteristic frequency of the process was higher than 1000 Hz.

7.2.3 E_a of LSCF-CGO composite cathode

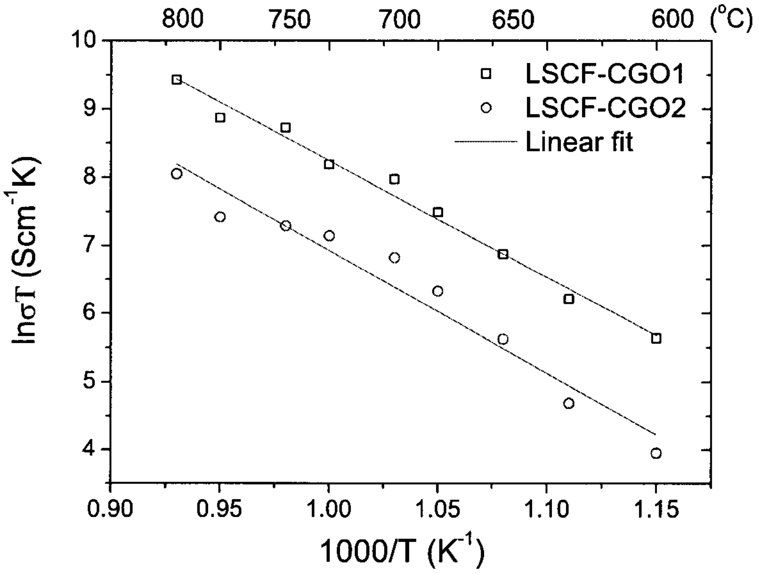

Figure 7.9: Arrhenius plots of LSCF-CGO composite cathodes.

Two LSCF-CGO composite cathodes were studied and the activation energy was analyzed by using the Arrhenius equation. The LSCF-CGO cathodes were made from different batches of precursor gel, which led to the LSCF loading variation in the composite layer. Fig. 7.9 shows the Arrhenius plots of LSCF-CGO cathodes from 600 to 800°C. The impedance spectroscopy of LSCF-CGO1 is shown in Fig. 7.4 and LSCF-CGO2 had similar spectra except that the high frequency arc was obscured. According to Fig. 7.9, the activation energy of the entire cathode reaction of LSCF-

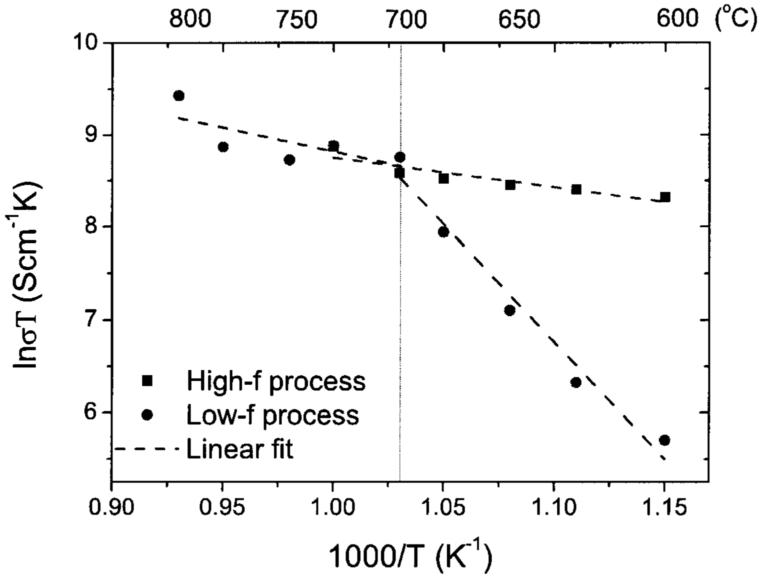

Figure 7.10: Arrhenius plots of the high and low frequency processes in LSCF-CGO composite cathodes between 600 and 800°C.

CGO1 and LSCF-CGO2 was calculated to be 1.48 and 1.55 eV, respectively.

Arrhenius plots of the high and low frequency processes of LSCF-CGO1 are shown in Fig. 7.10. Note that there is a sudden change of slope for the low frequency process at 700°C. E_a was calculated to be 2.17 and 0.45 eV below and above 700°C for the low frequency process. The activation energy of the high frequency process was calculated to be 0.28 eV below 700°C. Since the resistance of the high frequency part was relatively small and had minor change with increasing temperature after 700°C, E_a was negligible. A close examination of Fig. 7.9 showed that the slope of LSCF-CGO2 cathode also had a change at around 700°C. If E_a is calculated separately for the two parts, it is 0.93 eV and 2.11 eV for the high and low temperatures. The difference in E_a of the high and low frequency processes suggests that the low frequency process was the rate limiting step of LSCF-CGO composite cathode below 700°C. At temperatures higher than 700°C, an enhancement of the low frequency process was observed, which led to a sharp decrease of the activation energy, and thus the low and high frequency processes played an equal role in determining the cathode reaction rate. The details about the processes corresponding to each arc require further experiments to provide more information.

7.3 Cyclic Voltammetry

7.3.1 CV analysis for SOFCs

Over the past couple of decades, potential sweep techniques, such as cyclic voltammetry (CV), have been applied to an increasing range of systems to be used for preliminary mechanistic investigations. An electrochemical spectrum indicating the potentials at which processes occur can be rapidly obtained.

The potential-time waveforms used for sweep measurements are shown in Fig. 7.11. In linear sweep voltammetry (LSV), the electrode potential is swept from E_1 to E_2 at a fixed sweep rate. In cyclic voltammetry, the waveform is initially the same as in LSV, but on reaching the potential E_2, the sweep is reversed, instead of terminated. On again reaching the initial potential E_1, the potential sweep may be halted, again reversed or alternatively continued to a value E_3. In both the experiments, the current is recorded as a function of applied potential. In a typical qualitative study, it is usual to record voltammetry over a wide range of sweep rates and for various values of E_1, E_2 and E_3. It is possible to determine how the processes are represented by the peaks involved in the voltammetry. It is usually through observing how these peaks appear and disappear as the potential limits and sweep rate are varied, and by noting the differences between the first and subsequent cycles that the related processes are determined.

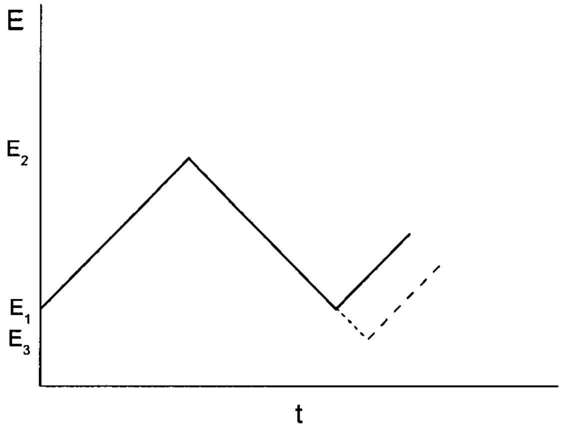

Figure 7.11: Potential-time profiles for sweep voltammetry.

7.3.2 Steady state study

A steady state study of the CMO-YSZ composite cathode was carried out using LSV with a potential scan rate of 1 mV/s. When the potential sweep rate is very slow, steady state response of the cathode can be obtained. Under steady state conditions, concentrations of the species involved in the reaction are maintained uniform above a certain distance from the electrode by natural diffusion.

Fig. 7.12(a) shows the steady-state polarization of CMO20-YSZ, CMO40-YSZ and CMO50-YSZ electrodes obtained at 700°C in air with a potential sweep from 0 to -300 mV. The magnitude of the observed current density in different cathodes from the lowest to the highest was in the sequence of CMO20-YSZ, CMO40-YSZ and CMO50-YSZ, which was governed by the polarization resistance of the cathodes. The potential-current density plots were linear and no limiting current density was observed. If charge transfer was the rate determining step, there would be a limiting current density due to the limitation of the oxygen ion exchange rate between the cat-

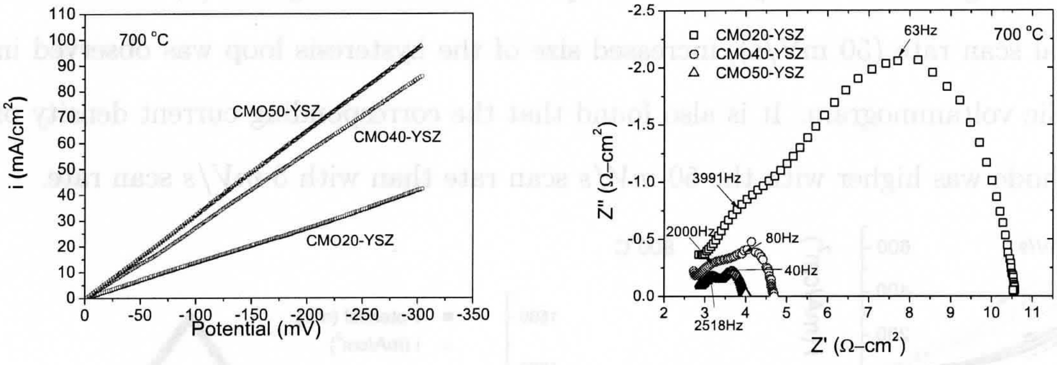

(a) (b)

Figure 7.12: (a)Steady state DC plot of CMO-YSZ cathodes at 700°C with a potential scan rate of 1 mV/s and (b) Corresponding impedance spectra for the cathodes at 700°C.

alyst and the electrolyte. As shown in Fig. 7.12(b), the low frequency arc dominated the impedance spectra of the CMO-YSZ cathodes, indicating that mass transfer was the rate determining step. Diffusion of oxygen may also have a strong influence on the reaction rate, which was discussed in Section 7.1.2. Fig. 7.12(a) revealed that as long as there was sufficient oxygen supply, the corresponding current density increased with the linear increase of the potential sweep. As a result, the steady state polarization plots of CMO-YSZ cathodes again demonstrated that charge transfer was not the rate limiting step at 700°C.

7.3.3 CV as a function of scan rate

By increasing the potential scan rate, the steady state condition cannot be maintained and the cathode reaction enters into an 'unstable' state. As shown in Fig. 7.13(a), the effects of potential scan rate on cyclic voltammograms of the CMO-YSZ composite cathode at 800°C were investigated. The applied potential sweep profile and the corresponding current density versus time plot are shown in Fig. 7.13(b). With a fast potential scan rate (50 mV/s), increased size of the hysteresis loop was observed in the cyclic voltammogram. It is also found that the corresponding current density of the cathode was higher with the 50 mV/s scan rate than with 5 mV/s scan rate.

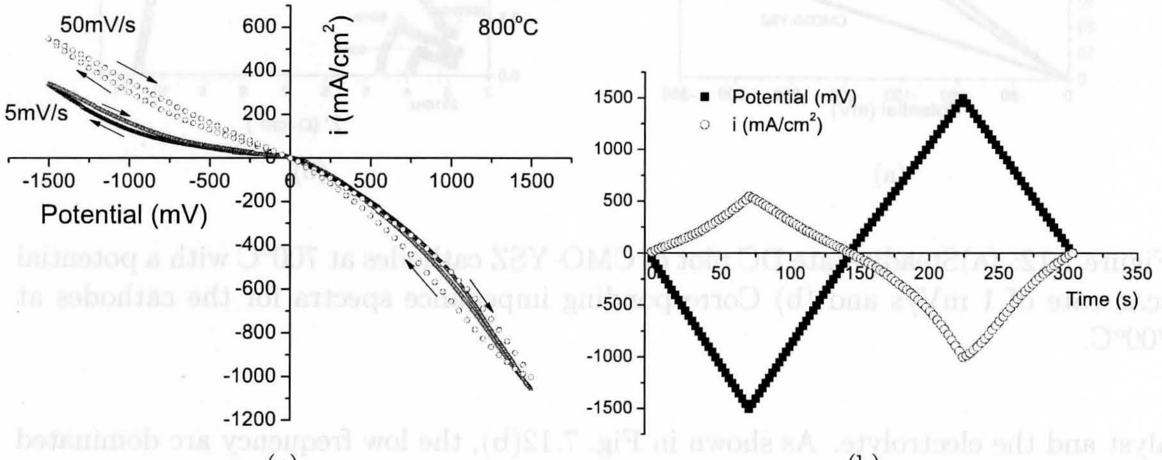

(a) (b)

Figure 7.13: (a)Effect of potential scan rate on the cyclic voltammograms of CMO-YSZ composite cathode at 800°C and (b) potential sweep profile and the corresponding current-time plot.

The transport of oxygen ions at the electrode/electrolyte interface is represented by the following reaction (Minh, 1995)(ERS: electrochemical reactive site):

$$O^{\times}_{O,ERS} \rightarrow O^{\times}_{O,YSZ} \tag{7.3}$$

If c^{c}_{O} and c^{YSZ}_{O} denote the concentration of $O^{\times}_{O,ERS}$ and $O^{\times}_{O,YSZ}$, respectively, the ratio of c^{c}_{O}/c^{YSZ}_{O} for a reversible system is given by the Nernst equation:

$$c^{c}_{O}/c^{YSZ}_{O} = \exp(\frac{zF}{RT}(E - E_0)) \tag{7.4}$$

It has been shown that for CMO-YSZ composite cathodes, surface diffusion is the rate determining step at temperatures above 750°C. From the starting potential to the first peak, as the potential is made more negative, the surface concentration of the reactant becomes progressively decreased, and hence the concentration gradient is increased and the current increases as well. Once this gradient exists, it does not remain constant but starts to relax owing to diffusion. At the same time, the electrode potential is still increasing, and therefore c_O^c is further decreased until it effectively reaches zero. If potential continues to increase, the current will decrease and a current peak appears. For a sweep rate of v, E can be expressed as follows:

$$0 < t < \lambda, E = -vt \tag{7.5}$$

$$t > \lambda, E = -2v\lambda + vt \tag{7.6}$$

where λ is the time at which the sweep is reversed. According to Equation 7.4, when a faster scan rate, v, is applied, it results in a larger concentration gradient of the oxygen ions, and therefore a larger current. This explains why a higher current density was observed for the CMO-YSZ composite cathode with a faster scan rate.

When the potential sweep is reversed, the current will directly track back through the forward path if the sweep rate is slow, which is steady state. For faster sweeps, there is a significant amount of $O_{O,YSZ}^{\times}$ present near the cathode and $O_{O,YSZ}^{\times}$ continues to be formed on the reverse sweep. The relatively slow diffusion of $O_{O,YSZ}^{\times}$ produced in the forward sweep close to the cathode/electrolyte interface causes extra oxygen ion concentration gradient in addition to the one induced by the applied potential sweep. As a result, an increased current density at the same potential value was observed compared with the forward scan. With a higher potential scan rate, the variation of potential is much faster compared with the diffusion of $O_{O,YSZ}^{\times}$, and thus the accumulated $O^{\times}_{O,YSZ}$ imposed an increased concentration gradient to the system, leading to a larger hysteresis loop appearing in the cyclic voltammogram with the 50 mV/s scan compared to the 5 mV/s scan.

The potential scan rate had a similar effect on the shape of hysteresis loops in the anodic scan as in the cathodic scan. However, the current response in an anodic scan was not a simple reversed process of the cathodic scan. Note that larger maximum current density and a more obvious difference in the shape of the hysteresis loops were observed in the anodic scan. The reason for this behaviour of the cathode is still under investigation.

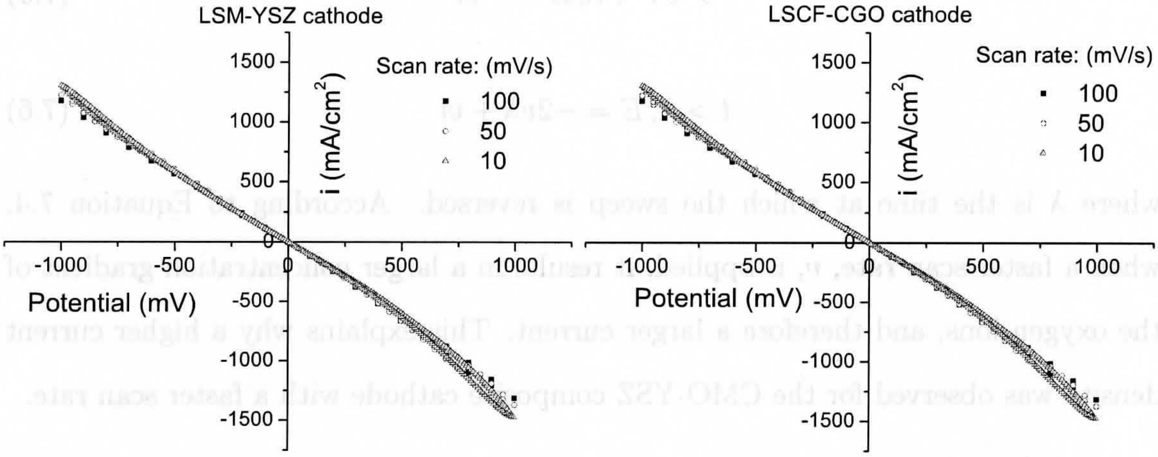

(a) (b)

Figure 7.14: Effect of potential scan rate on the cyclic voltammograms of (a) LSM-YSZ composite cathode and (b) LSCF-CGO composite cathode at 800°C. The potential sweep profile was similar to Fig. 7.13(b) but with the peak potential of ± 100 mV.

The effect of potential scan rates on CV plots for LSM-YSZ and LSCF-CGO composite cathodes were investigated as well. The potential sweep profile applied was similar to that shown in Fig. 7.13(b), but with a lower peak potential of ±1000 mV. Potential scan rates of 100, 50 and 10 mV/s were used in the CV measurements at

800°C. Fig. 7.14 revealed that the cyclic voltammograms of the perovskite composite cathodes had quite different behaviour from CMO-YSZ composite cathodes with variation of scan rate. Minor changes were observed for the CV plots with decreasing potential scan rate from 100 to 10 mV/s. Only a small hysteresis loop appeared in the anodic sweep with a scan rate of 10 mV/s. The insensitivity of the cyclic voltammograms with variation of scan rate suggested that surface diffusion wasn't the rate determining step for the perovskite-electrolyte composite cathodes at 800°C. It is possible that the oxygen diffusion rate in the electrolyte close to the LSM/YSZ and LSCF/CGO interface was much faster than the CMO/YSZ interface, so a steady state condition was maintained even under fast scan rate.

7.3.4 CV as a function of temperature

The effect of temperature on cyclic voltammograms of CMO-YSZ composite cathodes was investigated in the temperature range of 700 to 800°C with a potential scan rate of 50 mV/s, as shown in Fig. 7.15. No obvious hysteresis loop was observed in the cathodic scan at 700 or 750°C and the two plots almost overlapped. There was a small hysteresis loop in the cathodic scan at 800°C, in which the current density was much higher than at lower temperatures. Since mass transfer was shown to be the rate control process at lower temperatures, the same situation took place as in the steady state condition, at which the corresponding current just increased with the linear sweep of potential. At 800°C, oxygen ion diffusion became the rate determining step. The slow diffusion of oxygen ions at the electrode/electrolyte interface produced a higher concentration gradient on the backward scan, and as a result, increased current density at the same potential value was observed and a hysteresis loop appeared. The decreased current density at lower temperatures was due to increased polarization of the electrode with decreasing temperature.

In the anodic scan, hysteresis loops were observed at all temperatures. The oxygen ions were drawn from the YSZ electrolyte to the composite cathode under the anodic potential. The oxidation of the oxygen ions in the composite cathode is assumed to relate to the reduction of Mn^{4+} to Mn^{3+} and Cu^{2+} to Cu^{+}. The higher current density compared with the cathodic scan indicated that there was a significant gradient of $O_{O,YSZ}^{\times}/O_{O,ERS}^{\times}$ at the interface. The mechanism of the involved processes requires further exploration.

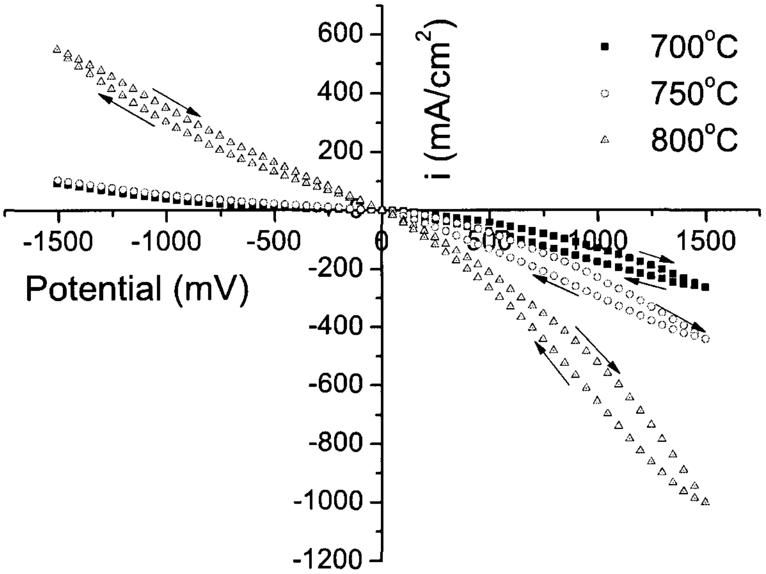

Figure 7.15: Effect of temperature on the cyclic voltammograms of a CMO-YSZ composite cathode with a potential scan rate of 50 mV/s.

7.4 Activation of the cathode under bias

The polarization performance of LSM has been found to be significantly improved by a passage of cathodic current. In our study, CMO-YSZ composite cathodes also showed enhanced catalytic activity after application of a cathodic current. The phenomenon of cathodic activation is a valuable tool to further investigate the mechanisms of the oxygen reduction reaction at the cathode. In order to get a better understanding of the activation of CMO-YSZ composite cathodes, mechanisms of the activation of LSM cathodes will be first reviewed.

7.4.1 Activation of LSM

The cathodic current enhancement effect for LSM has been widely studied. The activation effect of cathodic current passage on the polarization behavior of LSM electrodes has been attributed to the generation of oxygen vacancies, the enlargement of the three-phase boundary area, and the breaking of surface passive layers associated with SrO segregation.

The dramatic improvement of LSM catalytic performance under cathodic bias was recognized by Hammouche *et al.* (1991). Their study showed an apparent correlation among cathodic bias, oxygen deficiency and enhanced catalytic activity in LSM under large bias. They concluded that the cathode activation should result from the broadening of the active triple phase boundary area with increased ionic conductivity. Tsukuda & Yamashita (1994) attributed the activation phenomenon to a variation in cathode morphology from SEM observations on freshly prepared and polarized cells. They claimed that a change in microstructure of the cathode upon passage of the cathodic current enhanced the physical extent of triple phase boundary. vanHeuveln & Bouwmeester (1997) further pointed out that under reasonable current and potential bias, the activation was fully reversible, hence ruling out the possibility of non-reversible morphology or composition changes as the cause of activation. Jiang *et al.* (1999) observed the activation behavior of cathodes that had reacted with YSZ to form $La_2Zr_2O_7$ during fabrication, and were able to demonstrate that cathodic bias alone was insufficient to remove the insulating phase, thereby ruling out the hypothesis of interface modification under applied bias. Fig. 7.16 shows the electrode polarization resistance (R_E) of a freshly prepared LSM electrode as a function of time of cathodic current passage reported by Wang & Jiang (2004). They observed the microstructure change of LSM cathodes after cathodic and anodic current and ascribed the improvement of the cathodic performance to the breaking down of large agglomerates in freshly prepared LSM electrodes.

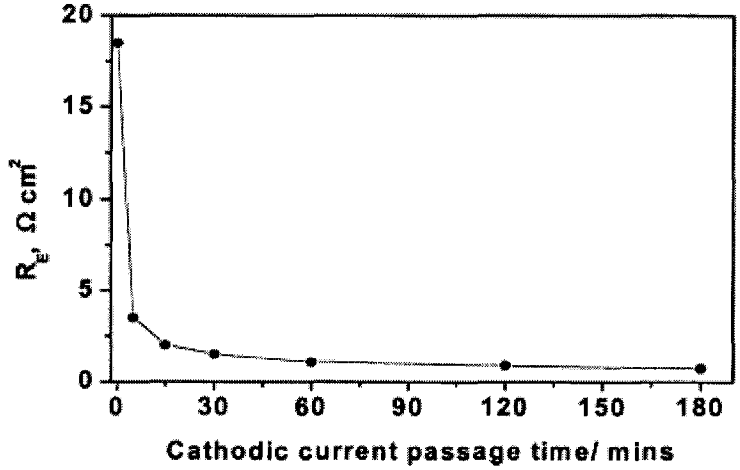

Figure 7.16: Electrode polarization resistance (R_E) of a freshly prepared LSM electrode as a function of cathodic current passage time at $200mA/cm^2$ and 800 °C in air. (Wang & Jiang, 2004)

There are several similarities and differences between LSM and CMO-YSZ composite cathodes. Considering common points, the two kinds of cathode both catalyze the oxygen reduction reaction, have a Mn^{3+}/Mn^{4+} redox couple and a porous microstructure. Regarding the differences, LSM has perovskite structure and CMO has spinel structure, and consequently different vacancy and cation distribution. LSM cathodes used in the previous study were only electronic conductors but the CMO-YSZ composite cathode can be regarded as a mixed ionic/electronic conductor. The similarities between the two helps to explain the activation process of the CMO-YSZ composite cathode with the aid of information derived from LSM cathodes, yet the differences cause CMO-YSZ cathodes to have activation behaviour different from LSM.

7.4.2 Activation of CMO-YSZ composite cathode

The cathodic current activation for the CMO-YSZ composite cathode was studied under constant applied current. Few studies have been reported on the current activation for the CMO-YSZ composite. The behaviour of the CMO-YSZ composite cathode under long-term cathodic and anodic current supply was studied by recording the variation of the polarization resistance and interfacial resistance as a function of time. Preliminary analysis of the activation and de-activation of the cathode was performed as well.

7.4.2.1 Cathodic current activation

The change of polarization resistance of a CMO20-YSZ composite cathode was studied at a current density of 252 mA/cm^2 at 800 °C in air. The duration for the current supply was 150 min. The applied current was paused from time to time to conduct impedance spectroscopy (IS) to measure the polarization resistance. The frequency range of IS measurement was from 0.01 Hz to 100 kHz and the signal amplitude was 10 mV. IS measurements were performed in a three-electrode arrangement at open circuit. According to the relatively small amplitude of the current in the IS measurement and the open circuit condition, it didn't introduce extra activation for the cathode.

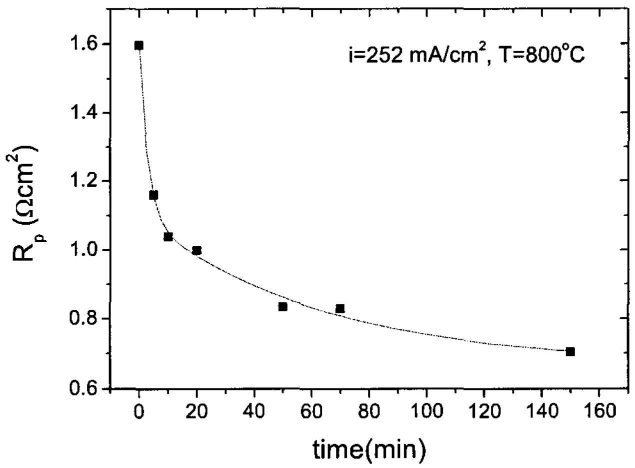

Figure 7.17: Polarization resistance of a freshly prepared CMO-YSZ composite cathode as a function of cathodic current passage time at 800 °C in air.

The variation of polarization resistance of the CMO20-YSZ cathode as a function of time is shown in Fig. 7.17. The polarization resistance of the freshly prepared CMO-YSZ composite cathode decreased with the application of the cathodic current. Rp showed a very sharp decrease in the first 10 min, after which the decrease in R_p was much slower with the current passage time. The initial R_p of 1.60 Ωcm^2 dropped to 1.03 Ωcm^2 after 10 min of current passage. After 150 min of cathodic polarization, Rp was reduced to 0.70 Ωcm^2. The results indicate that the activation process of cathodic bias on the polarization performance of CMO-YSZ cathodes was rather rapid and effective in the first 5 to 10 min of cathodic current passage under present test conditions.

The changes in the cathodic overpotential of a CMO40-YSZ cathode under constant current density was recorded with time at 800°C in air. Complete activation was assumed when constant current density was obtained. After activation, the current was switched off and the changes in interfacial resistance with time were monitored. Fig. 7.18 represents three typical activation-relaxation cycles obtained on a CMO-YSZ composite cathode. The interrupted current density applied to the cell was i=212 mA/cm^2 for 5 h with 19 h between each run.

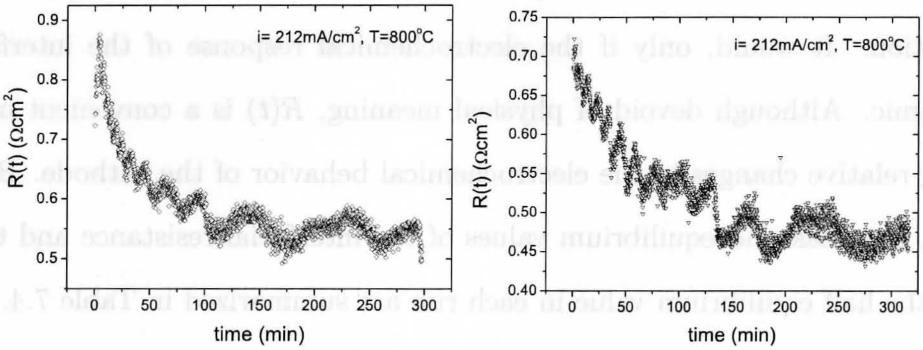

(a) 0 - 5 h

(b) 24 - 29 h

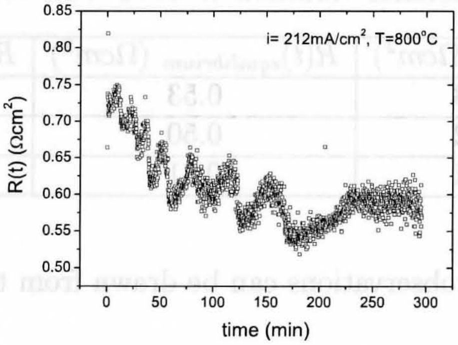

(c) 58 - 63 h

Figure 7.18: Three activation transients for a porous $Cu_{1.25}Mn_{1.75}O_4$-YSZ cathode at 800°C. The applied direct current was 212 mA/cm^2 with 19 h between each run. At time t = 0, the cathode was in its as-sintered state.

Martin (2007) proposed the following interfacial resistance, R(t), to describe the activation behaviour of the electrode in the overpotential measurement:

$$R(t) = \frac{\eta(t)}{i(t)} \tag{7.7}$$

$R(t)$ is defined as the ratio of the overpotential, $\eta(t)$, to the current density, i(t), in direct current regime, and therefore has the unit of Ωcm^2. $R(t)$ is independent from the current and potential bias conditions. It does not represent the local linearization $d\eta/di$ usually measured by impedance spectroscopy and therefore does not strictly correspond to the electrochemical impedance of the cathode at the (i, η) point under consideration. It would, only if the electrochemical response of the interface was purely ohmic. Although devoid of physical meaning, $R(t)$ is a convenient means of observing relative changes in the electrochemical behavior of the cathode. Based on Fig. 7.18, the peak and equilibrium values of the interfacial resistance and the time to reach the half equilibrium value in each run are summarized in Table 7.4.

Table 7.4: Interfacial resistance variation of CMO-YSZ cathode under activation.

	$R(t)_{peak}$ (Ωcm^2)	$R(t)_{equilibrium}$ (Ωcm^2)	$R(t)_{half}$	t_{half} (min)
0 - 5 h	0.88	0.53	0.70	16.21
24 - 29 h	0.72	0.50	0.61	25.59
58 - 63 h	0.74	0.61	0.68	27.03

Several qualitative observations can be drawn from the experimental results:

(1) The catalytic activity of the CMO-YSZ cathode was enhanced with the application of a cathodic bias. However, the activation effect for the CMO-YSZ composite was not as large as for the LSM cathode in the previous studies under similar conditions (e.g. Fig 7.16).

(2) The rate of the activation process, which was indicated by the time spent to reach half of the equilibrium resistance (t_{half}), slowed down in the second and third activation.

(3) After the first activation, full recovery of the initial interfacial resistance was

never achieved.

(4) Although the trend of the interfacial resistance was decreasing, oscillation of R(t) value was observed in the short time range.

(5) The first activation transient exhibited different kinetic behavior from the following ones, with an increase of $R(t)$ from 0.72 to 0.87 Ωcm^2 in the first 5 min, not present in the subsequent transients.

The relaxation of the cathode couldn't be recorded by the overpotential measurement, because the current supply was cut off to allow the relaxation between each activation. The change of the polarization resistance was recorded by impedance spectroscopy after the first and second activation to study the relaxation of the cathode, as shown in Fig. 7.19. Note that the polarization resistance obtained from impedance spectroscopy measurement was different from the interfacial resistance calculated from the overpotential measurement: they both represented the resistance of the interface but at open circuit and biased conditions, respectively. Yet the trend of the polarization resistance's variation represented the relaxation process as well. The initial polarization resistance of the CMO-YSZ cathode before all the activation processes was 0.56 Ωcm^2. The R_p value measured right after each activation was 0.26 and 0.24 Ωcm^2 for the first and second run. (R_p was measured as 1.077 Ωcm^2 after the third activation and the value indicated that physical damage had occurred in the cell. The cell was found to be cracked after cooling to room temperature.) R_p after 19 h relaxation was 0.57 and 0.63 Ωcm^2 in the first and second run. The relaxation of the polarization resistance indicated that the activation of CMO-YSZ composite cathode was reversible, similar to LSM. It was also observed that the polarization resistance after the second relaxation increased to 0.63 Ωcm^2 from the original

0.56 Ωcm^2. Fig. 7.19 further shows that the polarization resistance after the second activation was higher than after the first activation during the relaxation process. Possibly there were other processes competing with the cathodic current activation effect in the cathode, which increased the polarization. Final trend of the activation process requires the measurement for a even longer period of time.

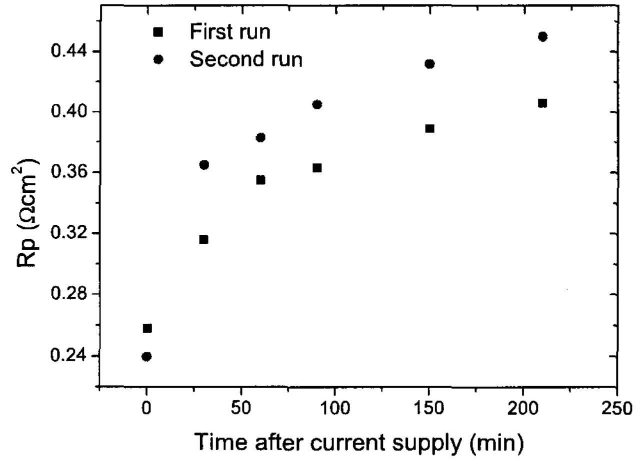

Figure 7.19: Relaxation of the CMO-YSZ cathode after activation.

7.4.2.2 Anodic current effect

The cathode behaviour under anodic current was also studied. Although it is believed that the anodic bias has a negative effect on the cathode performance, it is still of great interest to see whether the behaviour of the cathode under cathodic current supply was simply reversed or not. In the experiment, a constant current of -100mA/cm^2 was applied to a CMO20-YSZ cathode for 145 min. Note that there was no interruption to the current, and hence the recorded potential was the voltage of the entire cathode, including the ohmic response from part of the electrolyte. Since the potential response of the electrolyte was constant, it didn't influence the trend of the potential variation.

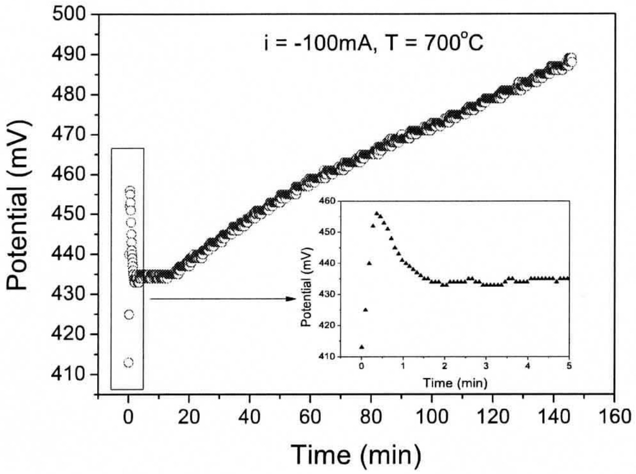

Figure 7.20: CMO-YSZ cathode potential variation under constant anodic current supply. The applied current density was -100 mA/cm^2 and the test condition was 700°C in air.

The variation of potential as a function of anodic current passage time can be characterized by three distinct regions as shown in Fig 7.20. A sharp increase of the potential was observed in the first 30 s of the current supply. Then the potential gradually decreased to 434 mV and stayed continuous for approximately 13 min. After that, the potential increased linearly with time at constant current supply. The results revealed it was not a simple reverse of the process under cathodic current supply. The results suggested that the anodic current eventually increased the polarization of the cathode but it possibly involved several processes, some of which even acted to enhance the cathode performance, according to the variation of the potential in the first 13 min. The increase of potential resulted from the increased polarization resistance with the anodic current passage, indicating a deactivation effect of anodic polarization on the oxygen reactions of the CMO-YSZ composite cathode.

Chapter 8

Summary and Conclusions

8.1 Summary

Gel impregnation is an alternative and effective technique in the development of the electrode structure to achieve high performance and an optimized microstructure. The effectiveness of the impregnation method in microstructure enhancement has been clearly demonstrated on the CMO impregnated YSZ cathode and LSCF-impregnated CGO cathode. With sufficient catalyst impregnation and suitable control of the sintering temperature, a connected network of catalyst particles formed in the electrolyte frame work, obtaining optimized microstructure. The impregnation method is proved to be effective in avoiding undesired phase during the fabrication process. Phase purity was achieved by sintering the catalyst at a lower temperature compared to the temperature at which the electrolyte matrix was sintered.

The polarization performance of the CMO-YSZ composite cathodes was investigated relating to the effect of CMO particle size, thickness of the functional layer and CMO content in the composite structure. Tanner's model was introduced to interpret the effects of the geometry parameters. 200 nm CMO particle size decreased the polarization of the cathode compared with 400 and 500 nm CMO particles. The critical thickness of CMO-YSZ composite layer was estimated to be 16.9±2.0 μm. Although there were experimental errors involved in the estimation, the CMO-YSZ cathodes having the closest thickness to the value of the critical thickness showed the lowest polarization loss compared with cathodes with a much thicker functional layer. With increased CMO content in the YSZ matrix, the length of the triple phase boundary was extended and the network of the electronic conductive phase was better connected, resulting in lower polarization at 50 wt% impregnation of CMO. The peak power density of the SOFC with CMO40-YSZ composite cathode was 172 mW/cm^2 at 800°C, about 2.5 time higher than the one with LSM-YSZ composite cathode. The decreased polarization loss and increase power density of CMO-YSZ cathodes compared with LSM-YSZ cathodes showed that CMO is an effective catalyst for the oxygen reduction reaction.

A clear understanding of the cathode reaction mechanism is of great importance in exploring new cathode materials. Impedance spectroscopy, equivalent circuit modeling, activation energy and cyclic voltammetry were used to study the rate determining steps of the cathode reactions at CMO-YSZ and LSCF-CGO composite cathodes. For CMO-YSZ composite cathodes, one or two arcs were observed in the impedance spectroscopy. The activation energy was approximately 1 eV for the high frequency process and from 1.5 to 2 eV for the low frequency process. Mass transfer was suggested to be the rate determining step at temperatures below 700°C and surface diffusion was believed to be the rate determining process at higher temperatures. Cyclic voltammetry results of CMO-YSZ cathodes further demonstrated the hypothesis on the rate determining steps. For LSCF-CGO composite cathodes, at least two rate determining steps existed and a significant decrease of the activation energy of LSCF-CGO cathodes above 700°C was observed for the low frequency process. In contrast to the case for CMO-YSZ composite cathodes, CV results indicated that surface diffusion was not the rate determining step for LSCF-CGO cathodes at high temperatures. The detailed processes corresponding to each arc haven't been determined.

Cathodic current activation effect was observed for the CMO-YSZ composite cathodes. The polarization performance of CMO-YSZ cathodes was improved by cathodic current passage. The polarization resistance dropped from 1.6 to 0.7 Ωcm^2 after 150 min cathodic current passage. The polarization resistance showed relaxation after the current supply was discontinued. Increased polarization of the cathode was observed under anodic bias but it was not a simple reversed process as under cathodic bias.

8.2 Conclusions

The following conclusions can be made from the study of the composite cathodes for SOFCs fabricated by the impregnation method:

(1) Gel impregnation is an effective method to fabricate SOFC cathode of optimized microstructure.

(2) CMO-YSZ composite electrodes have comparable cathode performance as traditional LSM-YSZ composite electrodes and show great potential to be used in ITSOFCs.

(3) Surface diffusion and mass transfer are the rate determining steps for CMO-YSZ

composite cathodes at high and low temperatures, respectively.

(4) The polarization of CMO-YSZ composite cathodes can be decreased by cathodic current activation.

(5) Preliminary study on LSCF-CGO cathodes reveals competitive performance as CMO-YSZ cathodes but with different reaction mechanisms.

8.3 Suggestions for future work

The dependance of impedance spectroscopy of CMO-YSZ composite cathodes on oxygen partial pressure should be investigated in order to further study the detailed cathodic reaction mechanism. Long-term stability measurement of the cathodes is of great importance to evaluate its potential application in ITSOFCs. The fuel supply conditions need to be optimized to increase the power density of the cells with CMO-YSZ composite cathodes. The preliminary study of LSCF-CGO composite cathodes suggests that the impregnation method overcomes the usually difficult sintering of LSCF/CGO system and shows great opportunity as a high efficiency ITSOFC cathode, and thus the oxygen reduction reaction mechanism in LSCF-CGO composite cathodes should be further explored.

Bibliography

Brett, Christopher M. A., & Brett, Ana Maria Oliveira. 1993. *Electrochemistry : principles, methods, and applications.* Oxford Science Publications.

Chen, C.C., Nasrallah, M.M., & Anderson, H.U. 1993. *Proceedings of the Third International Symposium on Solid Oxide Fuel Cells*, 252C266.

Fleig, J. 2003. Solid oxide fuel cell cathodes: Polarization mechanisms and modeling of the electrochemical performance. *Annual Review of Materials Research*, **33**, 361–382.

Hammouche, A., Siebert, E., Hammou, A., Kleitz, M., & Caneiro, A. 1991. Electrocatalytic properties and nonstoichiometry of the high-temperature air electrode $La_{1-x}Sr_xMnO_3$. *Journal of the Electrochemical Society*, **138**(5), 1212–1216.

Hansen, K.K., & Vels Hansen, K. 2007. A-site deficient $(La_{0.6}Sr_{0.4})_{1-s}Fe_{0.8}Co_{0.2}O_{3-\delta}$ perovskites as SOFC cathodes. *Solid State Ionics*, **178**, 1379–1384.

Huang, Q. A., Hui, R., Wang, B. W., & Zhang, H. J. 2007. A review of AC impedance modeling and validation in SOFC diagnosis. *Electrochimica Acta*, **52**, 8144–8164.

Huang, Y., Vohs, J. M., & Gorte, R. J. 2006. SOFC cathodes prepared by infiltration with various LSM precursors. *Electrochemical and Solid State Letters*, **9**(5), A237–A240.

Huang, Y. Y., Vohs, J. M., & Gorte, R. J. 2005. Characterization of LSM-YSZ composites prepared by impregnation methods. *Journal of the Electrochemical Society*, **152**(7), A1347–A1353.

Ivers-Tiffée, E., Weber, A., & Schichlein, H. 2003. *Handbook of Fuel Cells.* John Wiley.

Jerdal, L.O. 1998. *The Oxygen Electrode Process in Solid Oxide Fuel Cells.* Ph.D. thesis, NTNU.

Jiang, S. P., & Wang, W. 2005. Novel structured mixed ionic and electronic conducting cathodes of solid oxide fuel cells. *Solid State Ionics*, **176**(15-16), 1351–1357.

Jiang, S. P., Love, J. G., Zhang, J. P., Hoang, M., Ramprakash, Y., Hughes, A. E., & Badwal, S. P. S. 1999. The electrochemical performance of LSM/zirconia-yttria interface as a function of a-site non-stoichiometry and cathodic current treatment. *Solid State Ionics*, **121**(1-4), 1–10.

Jørgensen, M. J., & Mogensen, M. 2001. Impedance of solid oxide fuel cell LSM/YSZ composite cathodes. *Journal of the Electrochemical Society*, **148**(5), A433–A442.

Juhl, M., Primdahl, S., Manon, C., & Mogensen, M. 1996. Performance/structure correlation for composite SOFC cathodes. *Journal of Power Sources*, **61**(1-2), 173–181.

Kim, J. D., Kim, G. D., Moon, J. W., Park, Y. I., Lee, W. H., Kobayashi, K., Nagai, M., & Kim, C. E. 2001. Characterization of LSM-YSZ composite electrode by ac impedance spectroscopy. *Solid State Ionics*, **143**(3-4), 379–389.

Lu, C., Sholklapper, T. Z., Jacobson, C. P., Visco, S. J., & De Jonghe, L. C. 2006. LSM-YSZ cathodes with reaction-infiltrated nanoparticles. *Journal of the Electrochemical Society*, **153**(6), A1115–A1119.

Martin, Boris E. 2007. *The Performance of Perovskites and Spinels as Catalysts for Oxygen Reduction in Solid Oxide Fuel Cell Cathodes.* Ph.D. thesis, McMaster University.

Minh, N. Q. 1995. *Science and Technology of Ceramic Fuel Cells.* Elsevier.

Murray, E. P., & Barnett, S. A. 2001. $(La,Sr)MnO_3$-$(Ce,Gd)O_{2-x}$ composite cathodes for solid oxide fuel cells. *Solid State Ionics*, **143**(3-4), 265–273.

Murray, E. P., Tsai, T., & Barnett, S. A. 1998. Oxygen transfer processes in $(La_Sr)MnO_3/Y_2O_3$-stabilized ZrO_2 cathodes: an impedance spectroscopy study. *Solid State Ionics*, **110**(3-4), 235–243.

Odgaard, M., & Skou, E. 1996. SOFC cathode kinetics investigated by the use of cone shaped electrodes: The effect of polarization and mechanical load. *Solid State Ionics*, **86-8**, 1217–1222.

Østergård, M. J. L., & Mogensen, M. 1993. AC-impedance study of the oxygen reduction-checnism on $La_{1-x}Sr_xMnO_3$ in solid oxide fuel cells. *Electrochimica Acta*, **38**(14), 2015–2020.

Østergård, M. J. L., Clausen, C., Bagger, C., & Mogensen, M. 1995. Manganite-zirconia composite cathodes for SOFC: Influence of structure and composition. *Electrochimica Acta*, **40**(12), 1971–1981.

Petric, A., & Ling, H. 2007. Electrical conductivity and thermal expansion of spinels at elevated temperatures. *Journal of the American Ceramic Society*, **90**(5), 1515–1520.

Sholklapper, T. Z., Lu, C., Jacobson, C. P., Visco, S. J., & De Jonghe, L. C. 2006. LSM-infiltrated solid oxide fuel cell cathodes. *Electrochemical and Solid State Letters*, **9**(8), A376–A378.

Sholklapper, T. Z., Kurokawa, H., Jacobson, C. P., Visco, S. J., & De Jonghe, L. C. 2007a. Nanostructured solid oxide fuel cell electrodes. *Nano Letters*, **7**(7), 2136–2141.

Sholklapper, T. Z., Radmilovic, V., Jacobson, C. P., Visco, S. J., & De Jonghe, L. C. 2007b. Synthesis and stability of a nanoparticle-infiltrated solid oxide fuel cell electrode. *Electrochemical and Solid State Letters*, **10**(4), B74–B76.

Siebert, E., Hammouche, A., & Kleitz, M. 1995. Impedance spectrocopy analysis of $La_{1-x}Sr_xMnO_3$-yttria-stabilized zirconia electrode-kinetics. *Electrochimica Acta*, **40**(11), 1741–1753.

Singhal, S.C., & Kendall, K. 2003. *High Temperature Solid Oxide Fuel Cells-Fundamentals, Design and Applications.* Elsevier.

Skinner, S. J. 2001. Recent advances in Perovskite-type materials for solid oxide fuel cell cathodes. *International Journal of Inorganic Materials.*

Skou, E. M., & Jacobsen, T. 1989. A model for the frequency dispersion of the impedance of compressed powders of ionic conductors. *Applied Physics a-Materials Science and Processing*, **49**(1), 117–121.

Steele, B. C. H. 2000. Appraisal of $Ce1 - yGd_yO_{2-y/2}$ electrolytes for IT-SOFC operation at 500°C. *Solid State Ionics*, **129**(1-4), 95–110.

Tai, L. W., Nasrallah, M. M., Anderson, H. U., Sparlin, D. M., & Sehlin, S. R. 1995. Structure and electrical-properties of $La_{1-x}Sr_xCo_{1-y}Fe_yO_3$ .1. The system $La_{1-x}Sr_xCo_{1-y}Fe_yO_3$. *Solid State Ionics*, **76**(3-4), 259–271.

Tanner, C. W., Fung, K. Z., & Virkar, A. V. 1997. The effect of porous composite electrode structure on solid oxide fuel cell performance .1. Theoretical analysis. *Journal of the Electrochemical Society*, **144**(1), 21–30.

Tsukuda, H., & Yamashita, A. 1994. *Pages 715–724 of:* (ed), In: Bossel U (ed), *Proceedings of the first European solid oxide fuel cells forum.*

Tucker, M. C., Lau, G. Y., Jacobson, C. P., DeJonghe, L. C., & Visco, S. J. 2007. Performance of metal-supported SOFCs with infiltrated electrodes. *Journal of Power Sources*, **171**, 477–482.

Tucker, Michael C., Jacobson, Craig P., De Jonghe, Lutgard C., & Visco, Steven J. 2006. A braze system for sealing metal-supported solid oxide fuel cells. *Journal of Power Sources*, **160**(2), 1049–1057.

Van Herle, J., McEvoy, A. J., & Thampi, K. R. 1994. Conductivity measurements of various yttria-stabilized zirconia samples. *Journal of Materials Science*, **29**(14), 3691–3701.

Van Roosmalen, J. A. M., & Cordfunke, E. H. P. 1992. Chemical reactivity and interdiffusion of $(\mathrm{La,Sr})\mathrm{MnO_3}$ and $(\mathrm{Zr,Y})\mathrm{O_2}$, solid oxide fuel cell cathode and electrolyte materials. *Solid State Ionics*, **52**(4), 303–312.

vanHeuveln, F. H., & Bouwmeester, H. J. M. 1997. Electrode properties of Sr-doped $\mathrm{LaMnO_3}$ on yttria-stabilized zirconia .2. Electrode kinetics. *Journal of the Electrochemical Society*, **144**(1), 134–140.

Virkar, A. V., Fung, Kuan-Zong, & Tanner, Cameron W. 1996. Electrode design for solid state devices, fuel cells and sensors. *US Patent*, 5543239.

Virkar, Anil V., Chen, Jong, Tanner, Cameron W., & Kim, Jai-Woh. 2000. The role of electrode microstructure on activation and concentration polarizations in solid oxide fuel cells. *Solid State Ionics*, **131**(1-2), 189–198.

Wang, W., & Jiang, S. P. 2004. Effect of polarization on the electrode behavior and microstructure of $(\mathrm{La,Sr})\mathrm{MnO_3}$ electrodes of solid oxide fuel cells. *Journal of Solid State Electrochemistry*, **8**(11), 914–922.

Wang, W. S., Gross, M. D., Vohs, J. M., & Gorte, R. J. 2007. The stability of LSF-YSZ electrodes prepared by infiltration. *Journal of the Electrochemical Society*, **154**(5), B439–B445.

Xu, X. Y., Jiang, Z. Y., Fan, X., & Xia, C. R. 2006. LSM-SDC electrodes fabricated with an ion-impregnating process for SOFCs with doped ceria electrolytes. *Solid State Ionics*, **177**(19-25), 2113–2117.

Yamahara, K., Jacobson, C. P., Visco, S. J., Zhang, X. F., & de Jonghe, L. C. 2005. Thin film SOFCs with cobalt-infiltrated cathodes. *Solid State Ionics*, **176**(3-4), 275–279.

Youngblood, G. E., Rupaak, A. S., Pederson, L. R., & Bates, J. L. 1993. *Page 585 of:* Singhal, S. C., & Iwahara, H. (eds), *Proceedings of the first European solid oxide fuel cells forum.* The Electrochemical Society Proceedings, vol. PV 93-4.

Zhao, F., & Virkar, A. V. 2005. Dependence of polarization in anode-supported solid oxide fuel cells on various cell parameters. *Journal of Power Sources*, **141**(1), 79–95.